Precursor dynamical factors in the local lower atmosphere of Warm-Sector Heavy Rainfall over South China: Evidences from Wind Profiler Radar Observations

Wanju Li[1,2], Lifang Sheng[1], Xueyan Bi[2], Zehao Huang[3], Yali Luo[3], Shiqi Xiao[4], Chao Liu[3], Yang Yang[3], Jiandong Wang[3], Yuanjian Yang[3]*, Simone Lolli[5]

[1] College of Oceanic and Atmospheric Sciences, Ocean University of China, Qingdao, China
[2] Guangzhou Institute of Tropical and Marine Meteorology, China Meteorological Administration, Guangzhou, China
[3] State Key Laboratory of Climate System Prediction and Risk Management, School of Atmospheric Physics, Nanjing University of Information Science and Technology, Nanjing 210044, China
[4] School of Atmospheric Sciences and Key Laboratory of Tropical Atmosphere-Ocean System, Ministry of Education, Sun Yat-Sen University, Zhuhai, China
[5] CNR-IMAA, Contrada S. Loja, 85050 Tito Scalo (PZ), Italy

Correspondence to: Yuanjian Yang (yyi1985@nuist.edu.cn)

Abstract.

~~The~~ Warm-sector heavy rainfall (WSHR) is ~~one~~a type of intense convective precipitation that occurs far from the ~~most~~surface front under weak synoptic-scale forcing. It is a typical ~~weather events~~ type of heavy rain during the ~~early summer monsoon~~pre-flood season in South China ~~with instantaneous torrential rain with high locality and complex atmospheric conditions, which results in difficulties in nowcasting and hazard warning. Four dynamical~~, but due to its localized and sudden nature, forecasting skill remains limited. This study used observations from 14 wind profiler radar stations in Guangdong Province and hourly precipitation records from over 3,000 automatic weather stations (2016–2020) to identify 226 WSHR events across eastern, central, and ~~thermodynamical~~western Guangdong. Five indices ~~within~~reflecting the ~~lower~~ vertical structure of the atmosphere ~~are employed as precursor signals of WSHR over South China in 2019, including~~were analyzed in the three sub-regions — the Low-Level Jet Index (LLJI), ~~the~~ Vertical Wind Shear (VWS~~), the~~) at the 0.5–1.5 km and 1.5–3.0 km layers, Atmospheric Lifting Intensity (ALI), and ~~the~~ Boundary Layer Height (BLH~~), by utilizing wind profiler radar and high-density surface observations. Regional heterogeneity in~~). Notable fluctuations in signals were found 1 to 4 hours before precipitation onset, and the sensitivity and occurrence mechanisms of WSHR in the three regions showed marked regional differences. In western Guangdong, LLJI increased sharply within 1–2 hours before precipitation onset; although LLJI does not show a significant rank correlation with rainfall intensity, stratified analysis confirms that it is systematically higher in strong-rainfall events. LLJI was also significantly correlated with upper-level (3–5 km) ascent, indicating that the strengthening of the low-level jet can directly enhance upward motion and thereby increase precipitation intensity. In central Guangdong, VWS at 0.5–1.5 km was significantly positively correlated with precipitation intensity across three consecutive pre-onset periods, which may reflect frictional deceleration of the low-level jet over the Pearl River Delta and the resulting enhancement of low-level convergence. In eastern Guangdong, anomalously weak upper-level ascent and higher CAPE appeared before strong-rainfall events, indicating that suppressed mid-to-upper-level ascent allowed unstable energy to accumulate. Strong events were significantly warmer at 925 hPa, but showed no significant differences in large-scale vertical velocity or low-level relative humidity, suggesting that the instability accumulation was driven mainly by boundary layer warming; the anomalously high BLH is a manifestation of this thermal instability build-up. These regionally distinct precursor signals ~~are detected 1–4 hours preceding WSHR onset. Significant ALI and WVS signals in western regions are concentrated at approximately 1.5 km height, which is affected by warm, moist advection and orographic lifting. The central region, dominated by urban agglomerations, exhibited complex precursor signal interactions, where anomalies of LLJI and BLH are significant due to combined effects of urban heat island and the presence of the double LLJ at 1 km and 2.5 km, respectively. In contrast, precursor signals are moderated by the upper-level jet and moisture transport. In addition, monsoon activities and geographical factors play an important role in the spatiotemporal distribution of precursor signals. Urbanization effects on wind field at the boundary layer have significantly changed the features of dynamical precursor signals. The urban heat effect makes the low-level wind field more unstable. This research provides fundamental insights to enhance nowcasting and hazard warning~~provide an observational basis for developing sub-regional nowcasting guidance for WSHR in South China.

1 Introduction

The subtropical monsoon climate ~~prevails in~~dominates South China, where torrential ~~rainfall is one of~~rains are among the most ~~dominant~~frequent and impactful weather ~~events, especially~~ phenomena, particularly during the early summer monsoon season. Warm-Sector Heavy Rainfall (WSHR~~) is the most common~~), defined as intense precipitation that occurs 200–300 km ahead of the frontal boundaries of the surface on their "warm side" (Ding, 1994), is the most prevalent type of torrential rainfall during the summer monsoon in ~~South China (Ding, 1994), which usually denotes heavy rainfall occurring 200–300 km away from the front system at surface on its warmer side. This type of storm occurs in the~~ this region. These events typically develop in convergence ~~region of~~ zones between low-level flows in the southwest and southeast ~~in the lower troposphere or the southwest without significant~~ , often characterized by weak horizontal wind shear~~, which is free~~ and minimal influence from ~~the effects of~~ tropical ~~weather system such as Tropical Cyclones (TC)~~cyclones (Huang, 1986). ~~There is weak~~ Synoptic-scale baroclinic forcing and ~~atmospheric thermodynamical~~thermodynamic instability ~~at synoptic scale. Instantaneous and local torrential rainfall occurs under complex convective mechanisms under external forcings of rugged topography, thermodynamical and frictional contrast between land and sea, bringing challenges to forecast and reduction of natural hazard effects . There is limited performance of~~are generally weak, making the initiation of such extreme precipitation largely dependent on mesoscale convective processes modulated by complex terrain and land-sea contrasts (Sun et al., 2019). Consequently, numerical weather prediction models ~~from WSHR. Forecasts of precipitation~~ show limited skill in forecasting the timing, ~~regions~~location, and intensity ~~still need to be improved~~ of WSHR (Chen et al., 2019; Luo et al., 2017). ~~A recent study shows that there is limited~~ Convection-allowing ensemble experiments have shown that even very small differences in initial conditions can lead to divergent forecasts of warm-sector heavy rainfall, with the practical predictability ~~in WSHR events even with small initial errors, where~~closely linked to the accuracy of low-level ~~wind field can result in significant deviations among 3-hour forecast results~~winds over the sea and near-surface temperatures over coastal mountains (Wu et al., 2020). Therefore, observations of key meteorological ~~indices in higher~~variables at high spatiotemporal ~~resolutions~~resolution are ~~conductive~~critical to ~~higher~~improving accuracy of nowcast ~~accuracy in WSHR events~~.

~~Previous studies showed that WSHR in South China is highly associated with Low Level Jet (LLJ), where the convergence of low-level southerly is one of the most essential mechanisms for the occurrence of the WSHR near coastlines . The LLJ are typically classified into Surface LLJ (SLLJ) and Boundary Layer Jet (BLJ), which are relevant to the synoptic weather systems in the lower troposphere. Recent studies showed that the BLJ deaccelerates and converges, with the movement from the northern South China Sea to coastal South China due to the constrast of land-sea friction and coastal topography, coupled with the SLLJ in the lower-middle troposphere . This coupling results in strong mesoscale updraft, bringing warm and moist air from the ground to upper levels, which promotes the formation of strong convective precipitation.) developed a methodology to identify WSHR precursor signals at coastal regions in Guangdong Province by combining the LLJ, warm moist tongue and low-level convergence based on observational data and reanalysis data, which has been validated feasible. However, the false alarm in the hindcast experiments is due to the misidentification of vertical wind profiles. Therefore, the comprehensive study in vertical structures of the LLJ is conductive to extracting precursor signals, which improves the forecast performance in the WSHR. We used wind profiler radar data to analyze vertical profiles in high resolution right before the onset of WSHR events.~~

~~Wind profiler radar is a remote sensing instrument that operates at high altitudes without the need for balloons, It can provide instantaneous vertical wind speed profiles, particularly continuous wind profiles at middle-lower levels, especially into the boundary layer, with a temporal resolution of several minutes. . The wind profiler radar provides the horizontal wind speed, wind direction and vertical speed and atmospheric refractivity with a high vertical resolution with short delay, which permits to continuously monitor middle-lower wind field changes associated with mesoscale weather systems . Studies based on torrential rainfall events in Beijing, Shanghai, Guangzhou etc. show that the use of wind profiler radar can catch the evolution of a precipitation more efficiently, as the wind measurements can unveil changes of LLJ intensity, middle-lower level Vertical Wind Shear (VWS) and the wind fields, which grasps the occurrence of torrential rainfall.~~

~~Past research has primarily focused on a limited number of case studies or regional analyses, examining changes in LLJ, VWS, and other features. However, it has failed to present the spatiotemporal differences effectively. In this study, we select three wind profiler respectively deployed in western, central and eastern Guangdong Province to analyze evolutions of the BLH, VWS and wind speed in the cases of the WSHR events in 2019. Chapter 2 is descriptions of WSHR events in Guangdong~~

~~Province, data source and calculation diagnostics. Chapter 3 offers overview of each WSHR event. Chapter 4 shows analysis in spatiotemporal characteristics of precursor signals of WSHR events. Chapter 5 discusses possible mechanisms of transregional signal difference and applications of precursor signals in the WSHR forecast. Chapter 6 provides conclusions and discussion.~~

Previous studies have identified the low-level jet (LLJ) as closely associated with the formation of WSHR along the South China coast, where convergence of southerly low-level airflows favours convective initiation (Du et al., 2020a, b; Higgins et al., 1997; Stensrud, 1996; Trier et al., 2006; Zeng et al., 2019; Zhang and Meng, 2019). LLJs can be classified by their vertical position in the lower troposphere into synoptic-system-related low-level jets (SLLJs) and boundary layer jets (BLJs). Studies have shown that BLJs decelerate and converge as they move from the northern South China Sea toward the coast, influenced by land–sea frictional contrasts and coastal orography (Du et al., 2020b; Du and Chen, 2018; Zhang et al., 2022b), and interact with SLLJs to enhance mesoscale uplift and convective precipitation (Du and Chen, 2018; Du et al., 2020b). Zhang et al. (2022a) developed a promising method to identify precursor signals for WSHR by combining LLJ intensity indices, warm tongues, and low-level convergence using observational and reanalysis datasets. However, false alarms in forecasts are often caused by a lack of information on the vertical structure of the atmosphere. A thorough understanding of the pre-onset vertical structure of WSHR, enabled by high-resolution wind profiler radar (WPR) data, is therefore essential for accurate extraction of precursor signals and improved forecasting. WPR provide continuous, high-temporal and vertical-resolution measurements of horizontal and vertical wind components in the middle and lower troposphere, especially in the boundary layer, without reliance on balloon launches (Liu et al., 2020; Lolli et al., 2013; Kotthaus et al., 2023). These instruments have been increasingly used to investigate the evolution of LLJ, vertical wind shear (VWS), and atmospheric refractivity during torrential rainfall events in Beijing, Shanghai, and Guangzhou (Du et al., 2012; Li et al., 2024b; Xian et al., 2024; Zhou et al., 2022). Such high-resolution observations reveal dynamic changes in the low-level wind field preceding precipitation onset more effectively than conventional sounding data.

Despite progress, most previous studies have focused on limited case analyses or regional scales, lacking a detailed investigation of spatiotemporal differences in precursor signals. This study examines five lower-tropospheric precursor indices — the Low-Level Jet Index (LLJI), Vertical Wind Shear (VWS) at 0.5–1.5 km and 1.5–3.0 km, Atmospheric Lifting Intensity (ALI), and Boundary Layer Height (BLH) — during the pre-flood season (April–June) from 2016 to 2020, in order to improve the understanding of regional differences in the mechanisms of generation of WSHR.

The remainder of this paper is organized as follows. Sect. 2 describes the data sources and methods used in this study. Sect. 3 provides an overview of the WSHR events identified during the study period. Sect. 4 presents a comprehensive analysis of precursor signals, their temporal evolution, spatial characteristics, regional physical mechanisms, and urban effects. Finally, Sect. 5 summarizes the main conclusions and discusses implications for forecasting and future research.

2 Data and Methods

2.1 Data

~~The wind profile radar detects wind field variables primarily by the f electromagnetic wave scattering caused by the atmospheric turbulence. These variables include wind direction, horizontal wind speed, the atmospheric refractive index structure constant (C_n^2), vertical velocity, and more. This type of radar is divided into boundary layer wind profile radar (BWPR) and tropospheric wind profile radar (TWPR) depending on detection height. Th BWPR uses LC band within 0–6 km range, with a vertical resolution of 60 m, and a temporal resolution of 5 minutes. In contrast, TWPR utilizes the PA band for 0–16 km range, with a vertical resolution of 120 m, and a temporal resolution of 6 minutes. In this study, we used real-time sounding data (ROBS) and 1-hour c-averaged data (OOBS) from eight wind profiler radars in Guangdong Province, deployed at Chaozhou, Luogang, Zengcheng, Huadu, Conghua, Hailingdao, Zhuhai, and Xinhui. The instrument deployed at Luogang utilizes PA band, while the rest utilize LC band. Moreover, Luogang station data are interpolated to get 5-minute temporal resolution to be consistent with the temporal resolution of the LC band. Observations from 2550 high-density automatic weather stations in 2019 in Guangdong Province with 5-minute temporal resolution, including meteorological variables such as surface air temperature, air pressure, wind speed, wind direction, precipitation, etc. Locations of wind profiler radar, automatic weather stations and the distribution of urban impermeable subsurface are shown in Figure 1. The fifth-generation reanalysis dataset published by the European Centre for Medium-Range Weather Forecasts (ERA5) is used in this study to analyse Convective Available Potential Energy (CAPE) water vapor transport and weather backgrounds for diagnosis of water vapor conditions.~~

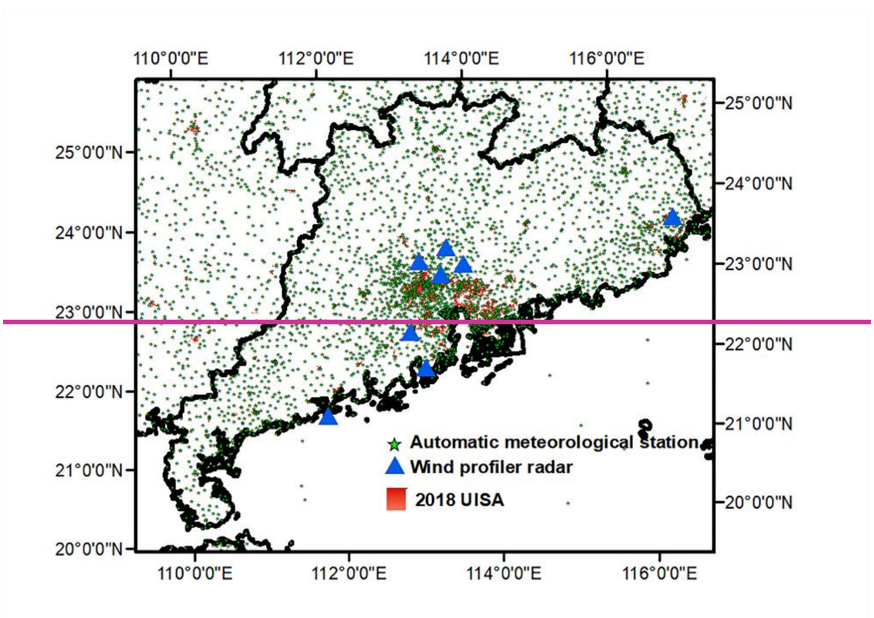

~~Figure : The distribution of wind profiler radars and high-density automatic weather stations in Guangdong Province is shown below. Red areas indicate urban subsurface areas (UISA). The locations of the wind profile radar stations are Hailing Island (HLD),~~ WPR continuously measure horizontal wind and vertical velocity profiles in the lower and middle troposphere at high temporal and vertical resolution (Liu et al., 2020), making them particularly suitable for studying the evolution of pre-precipitation wind fields associated with mesoscale weather systems. In this study, we used data from 14 WPR deployed throughout Guangdong Province during 2016–2020 (Fig. 1): boundary-layer wind profilers (BWPR, L–C band, 0–6 km, 60 m vertical resolution, ~6-min native temporal resolution) at most sites, and a tropospheric profiler (TWPR, P–A band) at Luogang (LG). The Guangdong Meteorological Administration provides two operational products: ROBS (real-time observation, raw profiles at the native resolution) and HOBS (half-hour observation, quality-controlled, 30-min effective resolution). All index calculations use HOBS, limited to 0–6 km due to reliability constraints at higher altitudes for L–C band systems. The 14 stations and their abbreviations are as follows:

Zhanjiang (ZJ), HaiLingDao (HLD), Luoding (LD), Xinhui (XH), Zhuhai (ZH), Nansha (NS), Huadu (HD), ~~Luogang (LG),~~ Conghua (CH), Luogang (LG), Zengcheng (ZC~~)~~), Shenzhen (SZ), Huizhou Longmen (HZ), Wuhua (WH), and Chaozhou (CZ).

All WPR data have undergone strict quality control. Records marked as invalid by the instrument were removed. Data exceeding 6000 m in range, horizontal wind speeds outside the range of 0–40 m s^{-1}, and vertical wind speeds outside the range of −10 to 10 m s^{-1} were also discarded. Subsequently, a two-dimensional median filter was applied in the time–height domain: for each data point, the median value of its valid neighbors within ±2 time steps and ±2 range gates was calculated. If there were at least three valid neighbors, any values that deviated from the median by more than 12 m s^{-1} (horizontally) or 5 m s^{-1} (vertically) were set to missing. This process effectively removed persistent contamination from ground clutter. After quality control, the overall availability of data during the analysis period was relatively high.

The number of high-density automatic weather stations (AWS) in Guangdong Province gradually increased between 2016 and 2020, reaching over 3,000 in 2020. This study used hourly precipitation data from over 3,000 AWS stations across the province to identify WSHR events and calculate precipitation weighted centroids. The locations of AWS stations and WPR, as well as the spatial distribution of urban pixels, are shown in Fig. 1. Urban extent in this study is characterised using the Local Climate Zone (LCZ) classification of Stewart and Oke (2012), with LCZ 1–10 (built-type classes) treated as urban pixels. LCZ maps for Guangdong Province are obtained from (Demuzere et al., 2022). This classification is used both for the province-wide visualisation in Fig. 1 and for the 3-km urban fraction reported per profiler station in Sect. 4.5 and Fig. 16 (areal percentage of LCZ 1–10 pixels within a 3-km buffer centred on each station).

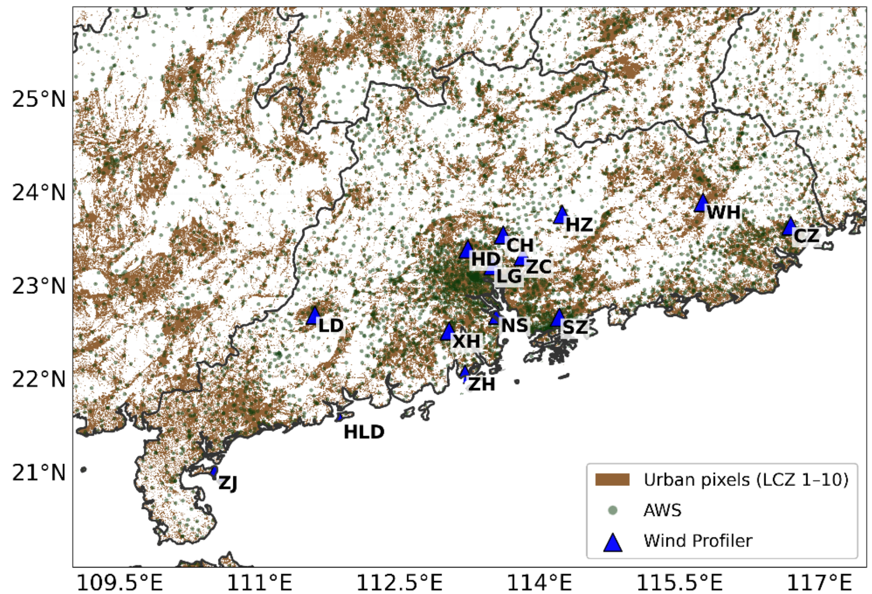

Figure **1: Spatial distribution of the WPR network (14 stations, blue), high-density automatic weather stations (>3000 sites, green), and urban pixels (LCZ 1–10, orange) in Guangdong Province.**

~~**2.2 Definition of the WSHR**~~

~~WSHR is defined as follows (Liu et al., 2019):~~

~~(1) Excluding typhoon-influenced precipitation;~~

~~(2) Daily precipitation of at least 50 mm is recorded at three or more neighboring stations (spaced ≤ 150 km apart);~~

~~(3) At least one consecutive 3-hour period with precipitation of at least 5 mm and at least one consecutive 3-hour period with rainfall of at least 30 mm recorded at each station.~~

~~WSHR events mostly occur under weak synoptic-scale forcing. Therefore, the condition that the precipitation is greater than 200 km away from the front must be satisfied for the WSHR. Eight WSHR events occurring in 2019 are selected according to these definitions.~~

Large-scale fields are obtained from the ERA5 reanalysis at 0.25° × 0.25° horizontal resolution and 1-hour temporal resolution, including geopotential height and winds at 925, 850, and 500 hPa, specific humidity for moisture transport and surface-based convective available potential energy (CAPE). Vertically~~and Dynamical Calculations~~

~~The physical mechanisms that trigger WSHR events can be ascribed to three mechanisms that characterize the torrential rainfall. The first mechanism is associated with thermodynamic instabilities, which can be identified using the BLH and the Atmospheric Lifting Index (ALI). The second is related to the dynamical processes identified using the ALI and VWS. In addition, we utilized the~~ integrated water vapor transport (IVT) is calculated between 1000 and 850 hPa as:

$$IVT_u = \frac{1}{g}\int_{1000\ hPa}^{850\ hPa} qu\ dp, \quad (1)$$

$$IVT_v = \frac{1}{g}\int_{1000\ hPa}^{850\ hPa} qv\ dp, \quad (2)$$

$$IVT = \sqrt{IVT_u^2 + IVT_v^2}\ , \quad (3)$$

where the IVT_u (IVT_v) are zonal (meridional) component of the moisture transport vector in kg m^{-1} s^{-1}, IVT is the magnitude of the vector, g is gravitational accelerations in m s^{-2}, u and v are zonal and meridional components of the layer-mean wind speed, respectively, q is the layer-mean specific humidity in kg kg^{-1}, and dp is pressure difference between two neighboring pressure levels. Positive values of IVT_u (IVT_v) indicate eastward (northward) zonal (meridional) components.~~to determine the magnitude and direction~~

In addition, vertical moisture transport profiles are characterized by each unintegrated term in Eq (4)–(6) for diagnosis in horizontal and vertical components for cross-sectional analysis of moisture transport~~. The wind profiler radar closest to the automatic stations recording the highest precipitation~~ :

$$VT_u = \frac{1}{g} qu\ , \quad (4)$$

$$VT_v = \frac{1}{g} qv\ , \quad (5)$$

$$VT_w = \frac{1}{g} q\omega\ , \quad (6)$$

where $VT_{u/v}$ are horizontal components of moisture transport in each vertical layer in kg m^{-1} s^{-1} Pa^{-1}, VT_w is vertical component of moisture transport in kg m^{-2} s^{-1}, ω is ~~chosen as~~ vertical components of velocity in Pa s^{-1}.

2.2 Definition and Selection of WSHR Events

WSHR events during the pre-flood season (primarily April–June) of 2016–2020 are identified in two stages. First, candidate warm-sector days are screened according to the method of Liu et al. (2019), which requires the following conditions to be met: (1) the influence of typhoons or tropical depressions is excluded; (2) the daily precipitation of three or more adjacent stations within 100 km is ≥50 mm, and there is a period of continuous 3 hours with hourly precipitation ≥5 mm and a 3-hour cumulative total ≥30 mm; (3) the warm-sector conditions are confirmed through vertical profiles of θ_{se} and temperature advection along the representative station longitude, that is: if there is no obvious frontal system on the profile, the precipitation area is dominated by southerly winds at low-to-middle levels, and the precipitation area is more than 200 km away from the nearest surface northerly wind; if there is an obvious frontal system on the profile, the precipitation area is more than 200 km away from the front. It should be noted that the detection capability of this method is limited by the density and distribution of the precipitation station network.

Secondly, individual events for each candidate day were objectively defined in three Guangdong sub-regions: western Guangdong (western GD, 21.0–22.5° N, 110.0–113.5° E), central Guangdong (central GD, 22.5–24.5° N, 112.5–114.5° E), and eastern Guangdong (eastern GD, 22.5–24.0° N, 115.0–117.0° E), as shown in Fig. 1. These regions correspond to ~~calculate atmospheric indices as~~ the main areas of high precipitation observed in the province's WSHR. For each sub-region and candidate day, hourly regional average precipitation was calculated from all AWS sites within the region. The onset of an event was defined as when the average precipitation rate reached or exceeded 1.0 mm h^{-1} for at least three consecutive hours. The event was considered to end after three consecutive hours below 1.0 mm h^{-1}; brief intervals of less than 3 hours were considered intra-event intervals. Events with a regional average cumulative precipitation of <5 mm were excluded. The precipitation weighted centroid was calculated as the cumulative precipitation weighted average of the station coordinates. For each event, the WPR station closest to the precipitation weighted centroid (limited to the same sub-region and ≤100 km away) was designated as the representative station for the precursor index calculation; events not meeting this condition were excluded from the analysis. Subsequent analysis (Sect. 4) focused primarily on precursor signals~~.~~ preceding precipitation, as precipitation particles and related contamination significantly degrade radar data quality after precipitation begins. The procedure generated a total of 226 independent WSHR events (65 in western GD, 88 in central GD, and 73 in eastern GD).

2.3 Indices of Atmospheric Conditions and Precursors

Based on the dynamic and thermodynamic conditions of precipitation, this paper selects five indices for study: LLJI, two VWS layers (0.5–1.5 km and 1.5–3.0 km), ALI, and BLH. These indices represent different physical processes—LLJ intensity, vertical shear structure, convective uplift, and boundary layer depth. Their relative importance in each region will be empirically assessed in Sect. 4. The indices were calculated from quality-controlled WPR data from representative stations for each event, at native ~30-min resolution and aligned with the precipitation onset time $t = 0$. Raw index values were winsorised at the 5th and 95th percentiles across all events before composite analysis to reduce the influence of extreme outliers. Sensitivity tests using non-winsorised data (not shown) produced consistent temporal patterns, indicating that the results are insensitive to this preprocessing choice.

2.3.1 Low-Level Jet Index (LLJI)

To quantitatively study the relationship between small-scale fluctuations in the LLJ and heavy rainfall, the LLJI is defined as (Liu et al., 2003):

$$I = \frac{V}{D},$$

~~(1~~(7)

where ~~V~~V is the maximum wind speed under 2 km altitude and ~~D~~D is the lowest ~~position of~~altitude at which the ~~12 m s⁻¹~~ wind speed reaches 12 m s^{-1} in a given time period. When the maximum wind speed does not reach 12 m s^{-1}, D is set to the altitude of the maximum wind speed. The downward transmission of the LLJ and the increase in wind speed leads to an increase in ~~I~~I. The precision of LLJI is limited by the WPR horizontal wind measurement uncertainty (~1–2 m s^{-1}) and the 60 m vertical resolution; in particular, winds below 0.5 km AGL are subject to ground clutter contamination and are therefore excluded from the computation.

2.3.2 Vertical Wind Shear (VWS)

The VWS of the horizontal wind is conducive to the baroclinic updraft within the convective system. Strong VWS tilts the convective updraft, enabling precipitation particles to fall out of the updraft region, thereby ~~allowing the hydrometeors in the updraft to separate from the updraft. This process prevents the weakening of the updraft~~reducing hydrometeor loading on the updraft and sustaining its buoyancy~~ due to drag effects.~~. Strong VWS ~~has been shown to enhance~~also enhances the entrainment of dry cold air into the middle layer, ~~strengthen~~strengthening the downdraft ~~in the storm,~~ and ~~the~~ cold outflow near the ground~~. This has~~, which forces the ~~effect of forcing the~~inflowing warm, moist air ~~flowing in~~ to rise more intensely~~ through forced uplifting. The result is an enhancement of convection and a facilitation of the coexistence of the updraft and downdraft for a considerable period of time.~~. The intensity of ~~the~~ VWS has a significant impact on the ~~organizational~~organisational structure of ~~the~~ convective ~~storm~~storms (single cell, multi-cell, and ~~super cell~~supercell). WSHR is closely related to the structure, ~~organization~~organisation, and propagation of ~~the~~ mesoscale convective ~~system (MCS),~~systems (Chen and Zhang, 2021) ~~Therefore, VWS is selected as one of the precursor signals of precipitation.~~. The following shows the formula of the VWS:

$$\cancel{\Delta V = \frac{\sqrt{(U_{z1}-U_{z2})^2+(V_{z1}-V_{z2})^2}}{(z1-z2)}}, \qquad \cancel{(2)}$$

$$\Delta V = \frac{\sqrt{(u_{z1}-u_{z2})^2+(v_{z1}-v_{z2})^2}}{(z1-z2)} \qquad (8)$$

where ΔV stands for the VWS (units: 10^{-3} s^{-1}), $\cancel{U_{z1}}u_{z1}$ and $\cancel{U_{z2}}u_{z2}$ represent zonal winds at heights z1 and z2, respectively, while $\cancel{V_{z1}}v_{z1}$ and $\cancel{V_{z2}}v_{z2}$ denote meridional winds at the top height z1 and the bottom height z2. VWS is analysed in two layers: 0.5–1.5 km (which spans the boundary-layer jet core) and 1.5–3.0 km (spanning the transition from the boundary-layer jet to the free troposphere). Wind measurements below 0.5 km are excluded from the layer-averaged VWS indices used in Sect. 4 due to ground clutter, although the full-resolution profiles shown in Fig. 7 retain this layer for descriptive purposes. The choice of the 0.5–1.5 km and 1.5–3.0 km layers is supported by the observed vertical shear maxima (Fig. 7) and typical boundary-layer jet core heights over coastal South China (Du and Chen, 2018).

2.3.3 Atmospheric Lifting Intensity (ALI)

~~It is well established that strong air uplift movements usually~~Strong upward motions are known to precede ~~the~~ precipitation onset. The product of the maximum uplift velocity and the thickness of the uplift layer is ~~therefore~~ calculated to quantify the intensity of the uplift $\cancel{N}ALI$:

$$\cancel{N}ALI = \cancel{W_{max} *} W_{max} \times H \cancel{*} \times 10 , \qquad \cancel{(3)} \qquad (9)$$

where H represents the atmospheric uplift ~~interval~~range where three consecutive observation altitudes within the 0–6 km altitude~~, when~~ range show upward vertical velocity~~ occurs in three consecutive observation altitudes~~; W_{max} represents the maximum vertical velocity ~~of~~(unit: m s^{-1}) within the atmospheric updraft ~~interval~~range. Factor 10 is a scaling constant used to adjust the index value to a range that is easy to display and compare. ALI values near and after the onset of precipitation should be interpreted with caution, as the vertical velocity measured by WPR contains contributions from hydrometeor fall speeds (~0.5–2 m s^{-1}) that cannot be separated from atmospheric ascent.

2.3.4 Boundary Layer Height (BLH) Estimation

~~The Boundary Layer Height (BLH) is a pivotal variable to describe the structure of the boundary layer , and it is crucial for elucidating turbulent motion. Furthermore, studies have demonstrated that wind speed is an important factor affecting the change of BLH . As a result, the height of the boundary layer is chosen as an early indicator. Both computational models and experimental findings have shown that the vertical distribution of the refractive index structure parameter, (C_n^2)peaks at the bottom of the top-covered inversion layer; this is where the humidity gradient is significant (Angevine).. As demonstrated, the method is employed to estimate the altitude of the top of the boundary layer. However, it is important to note that there is presence of clouds prior to the onset of precipitation, causing strong turbulent mixing in the clouds and entrainment mixing near cloud boundaries, resulting in higher C_n^2 than that at the top of the boundary layer. Furthermore, entrainment mixing in proximity to the cloud boundary has been observed to result in the occurrence of the peak of C_n^2 within the cloud. Therefore, it can be concluded that the joint use of the peak C_n^2 and the vertical wind speed variance σ_w^2 to estimate the BLH can improve the accuracy in the presence of clouds . In the mixed boundary layer, the heat flux exhibits a linear decrease in height from the ground to the upper boundary layer limit, reaching a minimum at the upper boundary layer. The vertical heat flux profile demonstrates a correlation with the standard deviation of the vertical velocity, which can be shown as:~~

$$\frac{\sigma_w^3}{z} \approx \alpha^{\frac{2}{3}} * \frac{g}{\theta} * \left(\overline{w'\theta_v'}\right), \tag{4}$$

~~where σ_w^2, z, and α denote the turbulent vertical velocity standard deviation, height, and generic constant (α =1.4), respectively, and $\frac{g}{\theta}\left(\overline{w'\theta_v'}\right)$ denotes the local buoyancy term, where g, θ, θ, and w' are the gravitational acceleration, the potential temperature, the virtual potential temperature, and the perturbed vertical velocity, respectively. It can thus be concluded that there is a relationship between the profile of the standard deviation of the vertical velocity and the profile of the atmospheric boundary layer sensible heat flux. The primary and secondary peaks are firstly selected in each C_n^2 vertical contour and the height of the peak near the ground surface is chosen as the estimated boundary layer height Z_1 following the relationship above; secondly, a linear regression line of Equation (4) is obtained by least-squares fitting of the previously estimated Z_1 and 0.2 Z_1. Finally, the height of the zero value of the heat flux, Z_0, is estimated by extrapolating the regression line, and the height of the peak C_n^2 closest to Z_0 is taken as the BLH.~~

Boundary layer height (BLH) is a key variable describing boundary layer structure (Seibert et al., 2000) and is crucial for elucidating turbulent motion. Furthermore, studies have shown that wind speed is a significant factor influencing BLH variation (Li et al., 2024a). Therefore, boundary layer height was chosen as a precursor indicator. BLH was estimated using an improved vertical velocity standard deviation (σ_w) method following Heo et al. (2003), who identified the convective boundary layer top from the altitude at which σ_w sharply decreases toward zero at the top of the turbulent layer using UHF wind profiler observations. The original joint C^2_n + σ_w implementation proposed in that work was simplified to the σ_w-o**nly** approach here, because reliable retrievals of the refractive-index structure parameter C^2_n were not consistently available across the 2016–2020 sample, particularly under weak-turbulence or dry boundary-layer conditions. Our implementation adapts the σ_w approach to the humid subtropical environment of coastal South China through layered σ_w computation (0–3000 m divided into 15 vertical bins of 200 m each), a gradient criterion between adjacent layers (Δσ_w/Δz), 3σ outlier removal, and recursive temporal smoothing of the 6-minute raw estimatesCompared to the standard method, this regional adaptation reduces the mean bias from +1524 m to +300 m (RMSE ~351 m at 20 BJT) when validated against the 2016–2019 April–June radiosonde data from Hong Kong Kings Park and Qingyuan stations. Although residual uncertainties of ±300–500 m remain typical for radar-based estimates in humid subtropical regions, the improved product reliably captures diurnal trends and relative changes preceding WSHR onset.

2.3.5 Calculation of vorticity and divergence

Based on the ~~‘~~triangle method (Bellamy, 1949)~~’, the~~, atmospheric vorticity and divergence can be calculated by using three ~~wind profile radar~~WPR stations deployed ~~into~~in a triangular shape (Wu et al., 2023). The component of each side of the triangle in the spherical coordinate system is calculated based on the latitude, longitude and earth radius at each vertex position of the triangle ($\triangle x_i, \triangle y_i, i = 1,2,3$). The divergence (~~D~~$D$) (unit: s^{-1}) and vorticity (~~ξ~~ξ) (unit: s^{-1}) can then be calculated at the same altitude by using the horizontal winds measured at the vertices ($u_i, v_i, i = 1,2,3$). The formulae are as follows:

$$D = \frac{(u_2-u_1)(\triangle y_3-\triangle y_1)-(u_3-u_1)(\triangle y_2-\triangle y_1)+(\triangle x_2-\triangle x_1)(v_3-v_1)-(\triangle x_3-\triangle x_1)(v_2-v_1)}{(\triangle x_2-\triangle x_1)(\triangle y_3-\triangle y_1)-(\triangle x_3-\triangle x_1)(\triangle y_2-\triangle y_1)},$$

~~(5)~~(10)

$$\xi = \frac{(v_2-v_1)(\triangle y_3-\triangle y_1)-(v_3-v_1)(\triangle y_2-\triangle y_1)+(\triangle x_2-\triangle x_1)(u_3-u_1)-(\triangle x_3-\triangle x_1)(u_2-u_1)}{(\triangle x_2-\triangle x_1)(\triangle y_3-\triangle y_1)-(\triangle x_3-\triangle x_1)(\triangle y_2-\triangle y_1)},$$

~~(6~~(11)

2.~~3.~~4 Statistical Methods

Composite time series are constructed by aligning all events at the beginning (t = 0) and computing the median value of each index in each time step. Uncertainty in the composite median is quantified using bootstrap resampling (2000 resamples with replacement); the 2.5th and 97.5th percentiles of the bootstrap distribution define the 95 % confidence interval.

Associations between index values and subsequent rainfall intensity are assessed using the Spearman rank correlation coefficient. Pre-onset values are averaged over four non-overlapping periods (t = –6 to –4 h, –4 to –2 h, –2 to –1 h, and –1 to 0 h) before computing the correlations. The boundaries of these periods are motivated by the composite wind field analysis (Sect. 4.1, Fig. 6), which identifies t ≈ −2 h as the onset of the most active pre-onset wind field evolution; the innermost period

(−1 to 0 h) also represents a practically relevant nowcasting lead time for WSHR. Significance is tested at the 95 % level ($p \leq 0.05$).

Regional differences in precipitation characteristics and precursor indices were tested using Kruskal–Wallis one-way ANOVA, with paired comparisons performed where appropriate. Strong and weak precipitation events within each subregion were demarcated by the median of the maximum hourly precipitation intensity recorded for each event; events above the median were classified as strong precipitation, and those below as weak precipitation. Differences between strong and weak precipitation event groups were assessed using the Mann–Whitney U test. All tests were two-tailed nonparametric tests. Sample sizes varied slightly across different figures because each analysis required continuous WPR data within different time windows; events with significant data gaps within the required windows were excluded. Exact numbers, determined independently for each analysis, are reported in the figure captions.

3 Overview of WSHR Events

Following the criteria defined in Sect. 2, a total of 226 WSHR events were identified in Guangdong Province during the pre-flood (April to June) of 2016–2020. The urban agglomeration of the Pearl River Delta (PRD) (hereafter the central GD) accounts for the largest share (88 cases, 39 %), followed by the Chaozhou–Shanwei coastal area in eastern GD (73 cases, 32 %) and the Yangjiang coastal area in western GD (65 cases, 29 %). Events peak in May–June across all three regions, though April events occur predominantly in the west.

The rainfall-weighted centroids of individual events cluster into three spatially separated groups (Fig. 2). The western events are concentrated along the coast near Yangjiang (21°–22.5°N, 110°–113°E), which faces the South China Sea to the south and is backed by the northeast–southwest-oriented Yunwu Mountains to the north. The trumpet-shaped topography near Yangjiang forces onshore airflow to converge and lift as it moves inland. Central events spread across the PRD (22.5°–24.5°N, 112.5°–114.5°E) and penetrate further inland than events in the other two regions. Eastern events are restricted to the Chaozhou–Shanwei coast (22.5°–24°N, 115°–117.5°E), bounded to the north by the Lianhua Mountains. The clear spatial gaps between the three clusters support the sub-regional classification adopted here; region boundaries are marked by the dashed rectangles in Fig. 2.

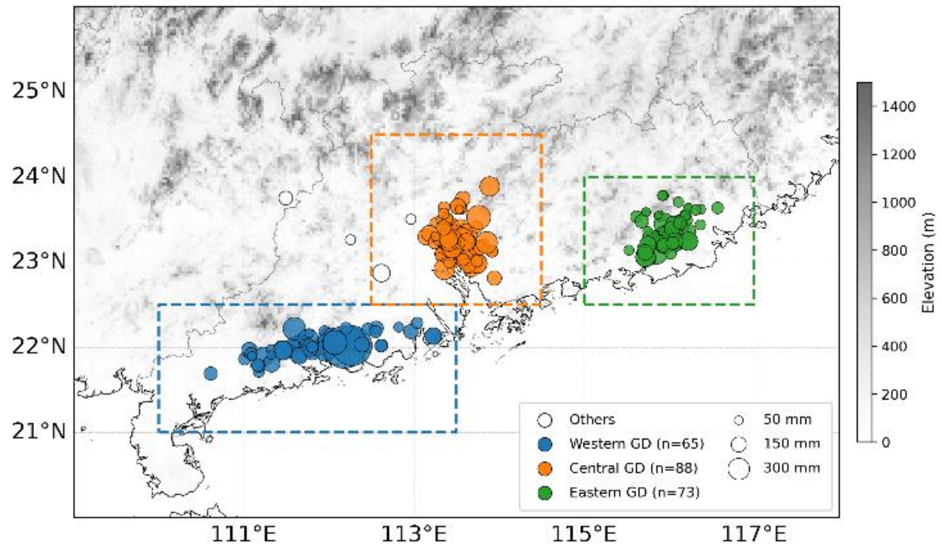

Figure 2: Spatial distribution of the WSHR precipitation centers in Guangdong Province during 2016–2020. The size of the marker is proportional to the maximum daily accumulated precipitation;white markers indicate invalid events. Dashed rectangles delineate the western (blue, n = 65), central (orange, n = 88), and eastern (green, n = 73) sub-regions. Gray shading shows the elevation of the terrain (m).

Among the four rainfall metrics examined (Fig. 3), only maximum hourly rainfall differs significantly across regions: the western median (~70 mm h^{-1}) substantially exceeds the eastern median (~55 mm h^{-1}), with the central region in between. This overall significance primarily reflects the contrast between the western and eastern regions. The mean intensity of the rainfall shows a weaker but still significant difference (H = 6.8, p = 0.03), while duration and total accumulated rainfall do not differ significantly between regions. Regional differences in WSHR are primarily reflected in rainfall intensity.

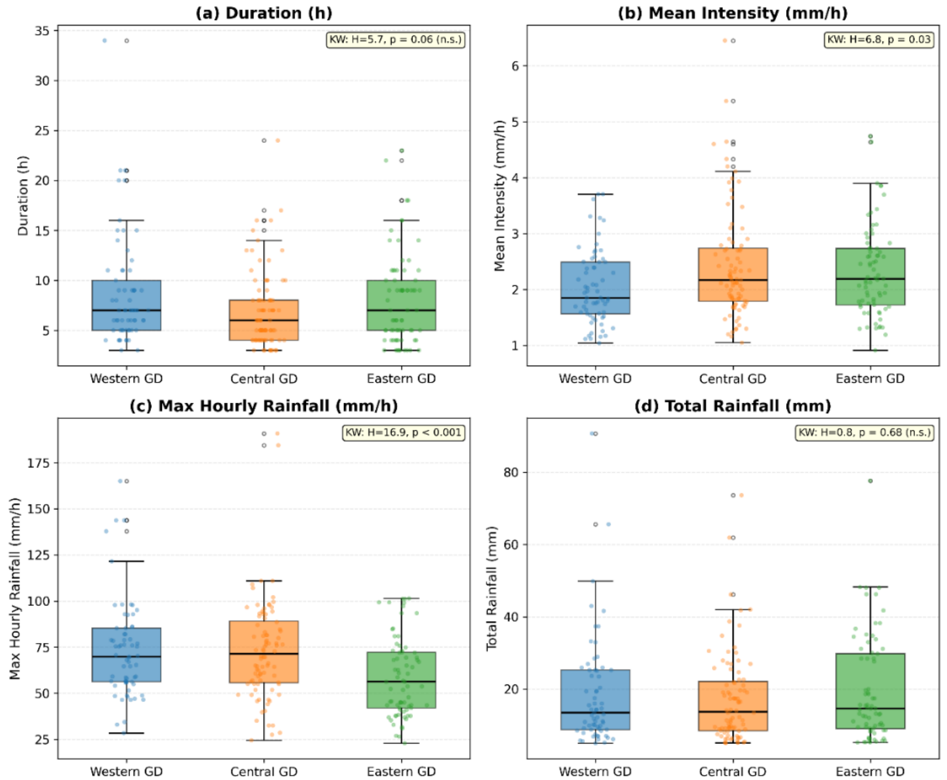

Figure 3: Statistical distributions of WSHR characteristics across three sub-regions: (a) event duration, (b) mean rainfall intensity, (c) maximum hourly rainfall, and (d) total accumulated rainfall. The boxes show the median and interquartile range; whiskers extend to 1.5 × IQR. The Kruskal–Wallis H statistic and the *p*-value are annotated in each panel.

Harmonic analysis of diurnal variations revealed distinctly different onset times across the three regions (Fig. 4a). All three regions exhibited a bimodal structure in their peak occurrence times, primarily in the early morning and afternoon, consistent with the diurnal variation characteristics of WSHR. In central GD, events were more concentrated in the afternoon (12:00–18:00 BJT, UTC+8), consistent with afternoon thermal forcing amplified by the urban heat island effect. Eastern GD showed a more pronounced morning peak (06:00–09:00 BJT), with nighttime acceleration and morning deceleration of the boundary layer jet likely triggering factors. Western GD exhibited a bimodal distribution: a secondary peak occurred near 03:00–05:00 BJT, while the main peak was at 12:00–15:00 BJT, possibly stemming from the superposition of nighttime land breeze convergence and afternoon solar heating enhanced by coastal topography.

However, the combined S1 + S2 harmonics only explained 18%–25% of the total variance in onset times across the three regions. Weather-scale variability remains the dominant factor controlling when individual events trigger. This limitation is more evident in precipitation intensity analysis (Fig. 4b): although the diurnal variation of intensity in western and eastern GD is roughly consistent with its onset time, central GD shows an almost flat intensity cycle (S1 + S2), indicating that the precipitation intensity over urban agglomerations is jointly influenced by synoptic-scale water vapor supply, mesoscale convergence and local boundary layer processes, rather than being controlled solely by diurnal thermodynamic cycles.

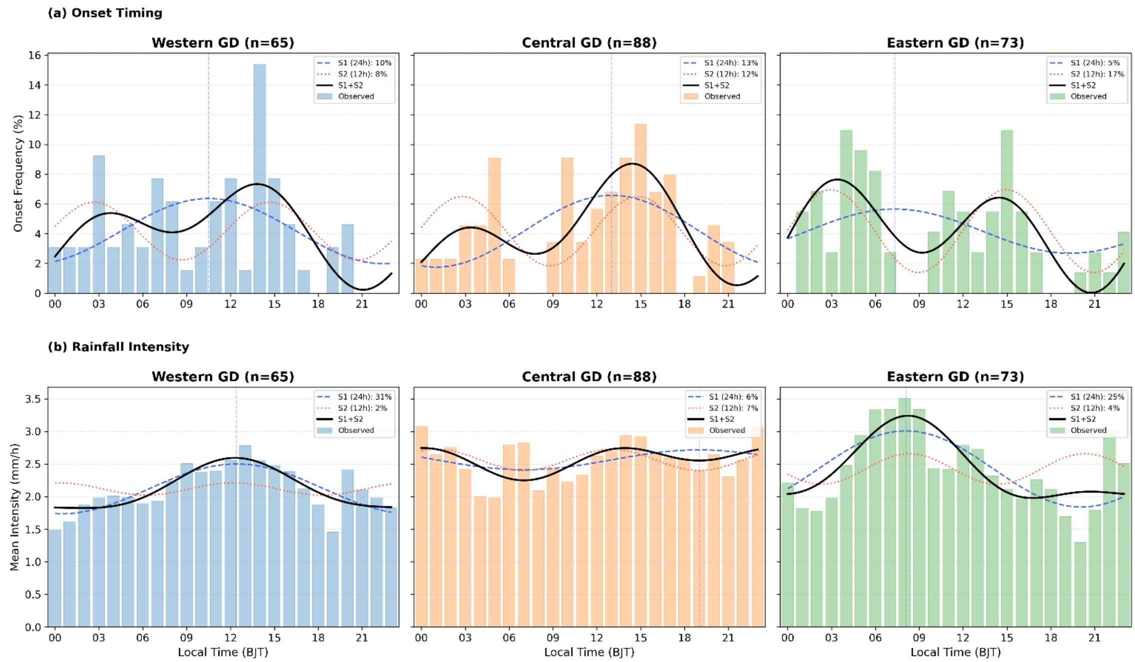

Figure 4: Diurnal variations of (a) WSHR onset frequency and (b) mean rainfall intensity for the western (blue), central (orange), and eastern (green) regions. The dashed and dotted curves show the first (S1, 24 h) and second (S2, 12 h) diurnal harmonics; solid black curves show S1 + S2. Percentages indicate explained variance.

Composite synoptic fields (Fig. 5) reveal the large-scale environment at the time of the WSHR events in the three regions. The most significant differences occur at 925 hPa (Fig. 5g–i). In central and eastern GD, LLJs greater than 8 m s^{-1} extend from the South China Sea deep into the inland waters of GD, reaching the PRD in central GD and traversing the entire Chaoshan coastline in the eastern composite. The pattern in central GD is consistent with the coupling between BLJs and SLLJs recorded by Du and Chen (2018) and Du et al. (2020a). In contrast, the western GD composite shows lower wind speeds over Guangdong and the low-level jet confined to nearshore waters, barely penetrating inland. At 850 hPa (Fig. 5d–f), this contrast persists: a well-defined LLJ extends from the northern South China Sea deep into Guangdong for the central and eastern composites, whereas the western composite shows a considerably weaker jet signal limited to coastal waters. At 500 hPa (Fig. 5a − c), the subtropical high ridge axis lies south of 20° N for all three regions. The western composite shows the ridge axis positioned slightly further north and east compared to the central and eastern composites, placing western GD marginally closer to the northern flank of the anticyclone. In the central and eastern composites, Guangdong lies more squarely under the south–southwestern periphery of the high, with the associated southwest to south flow providing a more direct pathway for moisture transport ~~calculation and diagnosis of vertical~~ into the region.

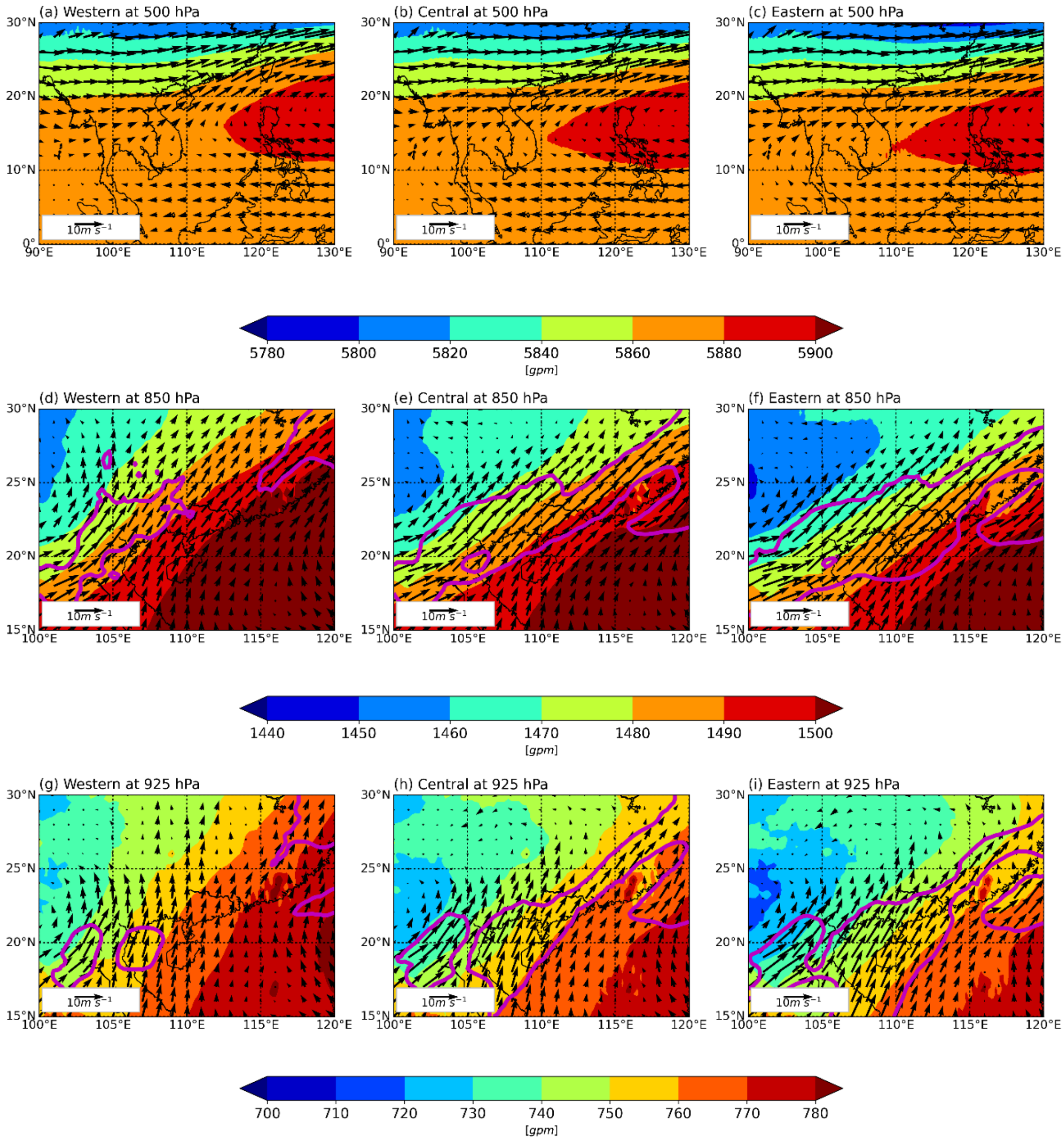

Figure 5: Composite mean geopotential heights and wind field at 500 hPa (a–c), 850 hPa (d–f) and 925 hPa (g–i) over WSHR events in Western (a, d, g), Central (b, e, h) and Eastern (c, f, i) GD. Geopotential heights in gpm, wind vectors (black arrows) in m s^{-1} with wind speed greater than 8 m s^{-1} marked in magenta contours.

In summary, the composite analysis indicates that the three sub-regions are associated with different large-scale environments, dominant onset times, and precipitation intensity distributions. Events in western GD are characterized by the strongest peak hourly precipitation, but large-scale jet forcing is relatively weak, and low-level airflow is mainly confined to the nearshore area. Events in central GD are the most frequent, tending to peak in the afternoon, and occur under conditions of a dual low-level jet structure over the PRD. Events in eastern GD are most common in the early morning, and are associated with the most extensive low-level jet penetrating into the coastal zone. These contrasting characteristics observed in the pre-precipitation weather environment and diurnal variation behavior prompt a more detailed examination of the local wind field evolution in the hours leading up to the onset of WSHR, which is the focus of Sect. 4.

4 Precursor Signal Characteristics and Mechanism Analysis

Sect. 3 characterised the synoptic-scale environments in which the three types of WSHR events are embedded. This section shifts focus to the local lower-tropospheric wind field, as observed by WPR in the hours surrounding precipitation onset. All events are aligned so that the onset time is $t = 0$; composite statistics are computed for the window $t = -6$ h to $t = +3$ h. For each event, the profiler station nearest to the rainfall-weighted centroid (Sect. 2) serves as the representative station. Vertical velocity measurements were pre-processed following the quality control procedure described in Sect. 2.

4.1 Wind field evolution in the hours before onset

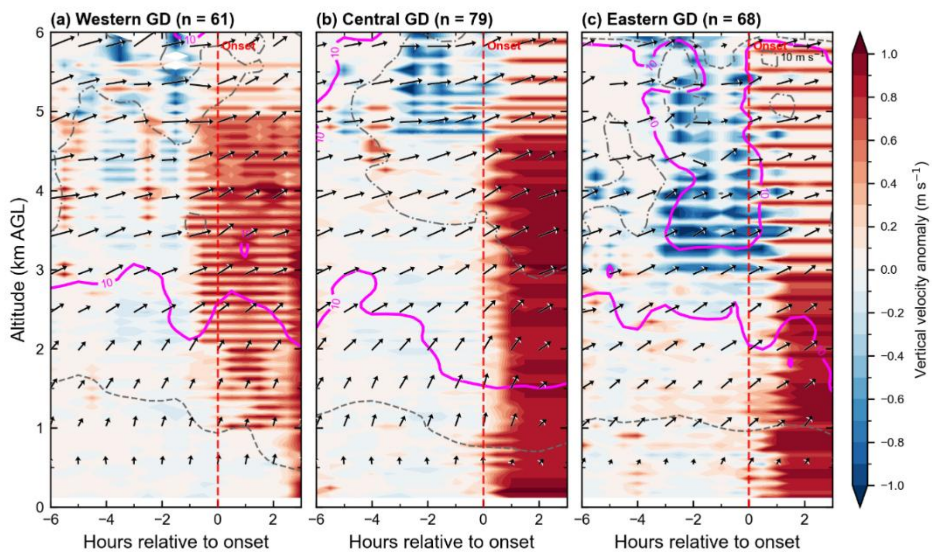

Figure 6: Composite time–height cross-sections of horizontal wind and vertical velocity anomalies for (a) western GD (n = 61), (b) central GD (n = 79), and (c) eastern GD (n = 68) WSHR events. Arrows show composite wind vectors (reference: 10 m s^{-1}); shading shows the median vertical velocity anomaly relative to the t = −6 to −4 h baseline (m s^{-1}; red for ascent, blue for descent); magenta contours mark 10 m s^{-1} wind speed. The gray contours with dashed and solid lines indicate 8 and 12 m s^{-1}, respectively. The red dashed line indicates onset (t = 0).

Fig. 6 presents composite time–height cross-sections of horizontal wind and vertical velocity anomalies for the three regions. The vertical velocity anomaly is defined as the departure from the median over $t = -6$ to -4 h at each height level, thus removing the instrument-related background and highlighting the changes associated with approaching convection. Two features are shared in all three regions: (i) a progressive strengthening of low-level winds in the hours before onset, and (ii) a transition from near-zero to positive vertical velocity anomaly beginning 1 to 3 h before onset.

In western GD (Fig. 6a), southerly winds prevailed below 2 km before precipitation, shifting clockwise to westerly winds above 3 km, consistent with low-level warm advection. Several hours before precipitation, wind speeds gradually increased at the 2–4 km level, with significant fluctuations in the 10 m s^{-1} contour around $t = -2$ h. In central GD (Fig. 6b), the low-level jet began to descend around $t = -4$ h, with winds exceeding 12 m s^{-1} appearing above 3.5 km several hours before precipitation. After the onset of precipitation, the vertical ascent signal was the strongest among the three regions, with positive anomalies rapidly expanding upward. In eastern GD (Fig. 6c), the wind field is more vertically uniform: south-southwest winds extend from the surface to above 3 km with modest directional shear. The low-level jet persists steadily near 2–3 km throughout the pre-onset period. A notable feature is the negative vertical velocity anomaly at 3–5 km during $t = -3$ to 0 h, indicating a mesoscale suppression of ascent in the middle troposphere prior to onset, followed by a positive anomaly that develops below 3 km and intensifies through onset.

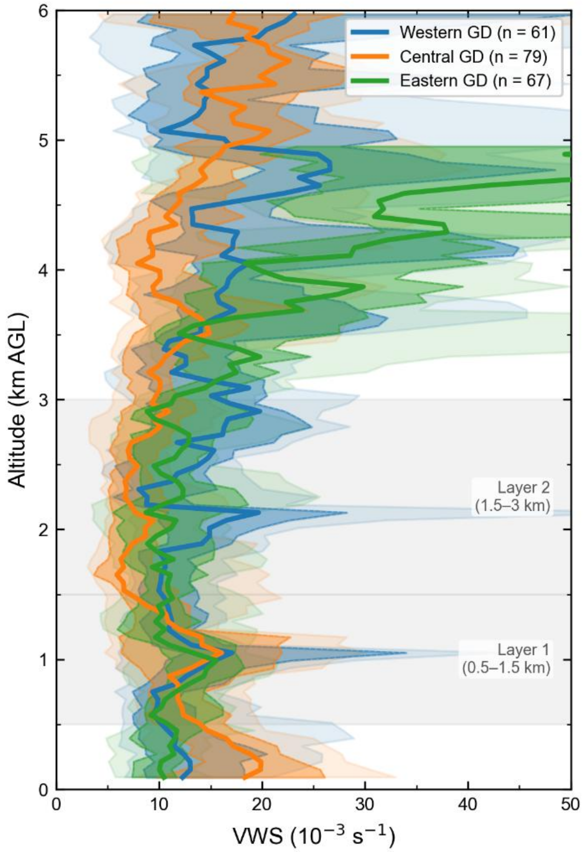

Figure 7: Composite VWS profiles averaged over $t = -3$ to 0 h for the western GD (blue, $n = 61$), central GD (orange, $n = 79$), and eastern GD (green, $n = 67$) regions. Lines show medians; dark and light shading show the 25-75 percentile range and 10th–90th percentile ranges. The gray bands mark the two layers used in Sect. 4.2: 0.5–1.5 km (Layer 1) and 1.5–3.0 km (Layer 2).

~~Moisture transport is one of the most important proxies to characterize the dynamic moisture processes to form precipitation. In this study, we utilized ERA5 data to calculate the IVT from 850 hPa to 1,000 hPa using Eulerian framework.~~

$$\cancel{= \frac{1}{g}\int_{1000\,hPa}^{850\,hPa} qu\,dp\,,} \qquad \cancel{(7)}$$

~~IVT_v~~The composite VWS profiles (Fig. 7) quantify the vertical shear structures in the pre-onset period. VWS is computed between adjacent 60 m range gates and averaged over $t = -3$ to 0 h; this window is chosen because it encompasses the period of most active pre-onset wind field evolution identified in Fig. 6.

Three local VWS maxima are identified below 3 km in all regions. The first maximum occurs below 0.5 km and is more pronounced in the central GD (median ~$20 \times 10^{-3}\ s^{-1}$), reflecting the strong near-surface wind gradient over the PRD surface. The second maximum lies in the 0.5 to 1.5 km layer and is present in all three regions, corresponding to the wind speed gradient between the surface layer and the jet core. The third maximum, in the 1.5 to 3.0 km layer, is strongest in eastern GD.

These three maxima motivate the choice of analysis layers for Sect. 4.2: 0.5–1.5 km (Layer 1, capturing BLJ-related shear) and 1.5–3.0 km (Layer 2, capturing the BLJ–free-troposphere transition). The lower bound of 0.5 km is adopted because profiler measurements in the lowest few hundred meters are subject to ground clutter and large frictional variability (Liu et al., 2020). The upper bound of 1.5 km encompasses the jet core, which typically resides near 1 km over coastal South China (Du and Chen, 2018).

In summary, the composite analysis reveals coherent pre-onset signals across all three regions—progressive low-level wind intensification, a transition from suppressed to enhanced ascent, and distinct vertical shear layering—but with regional differences in timing, vertical structure, and magnitude. To quantify these signals systematically, Sect. 4.2 examines the temporal evolution of five precursor indices.

4.2 Temporal evolution of precursor indices

To quantify the pre-onset signals identified in Sect. 4.1, composites of precursor indices are constructed for each region (Fig. 8). Five quantities are examined: LLJI, VWS at 0.5 to 1.5 km and 1.5 to 3.0 km, ALI, and BLH. All indices are computed at 30 min resolution and aligned by onset time. In each panel, the solid line shows the composite median, and the dark shading indicates bootstrap 95 % confidence interval of the median (2000 resamples), and the light shading shows the interquartile range.

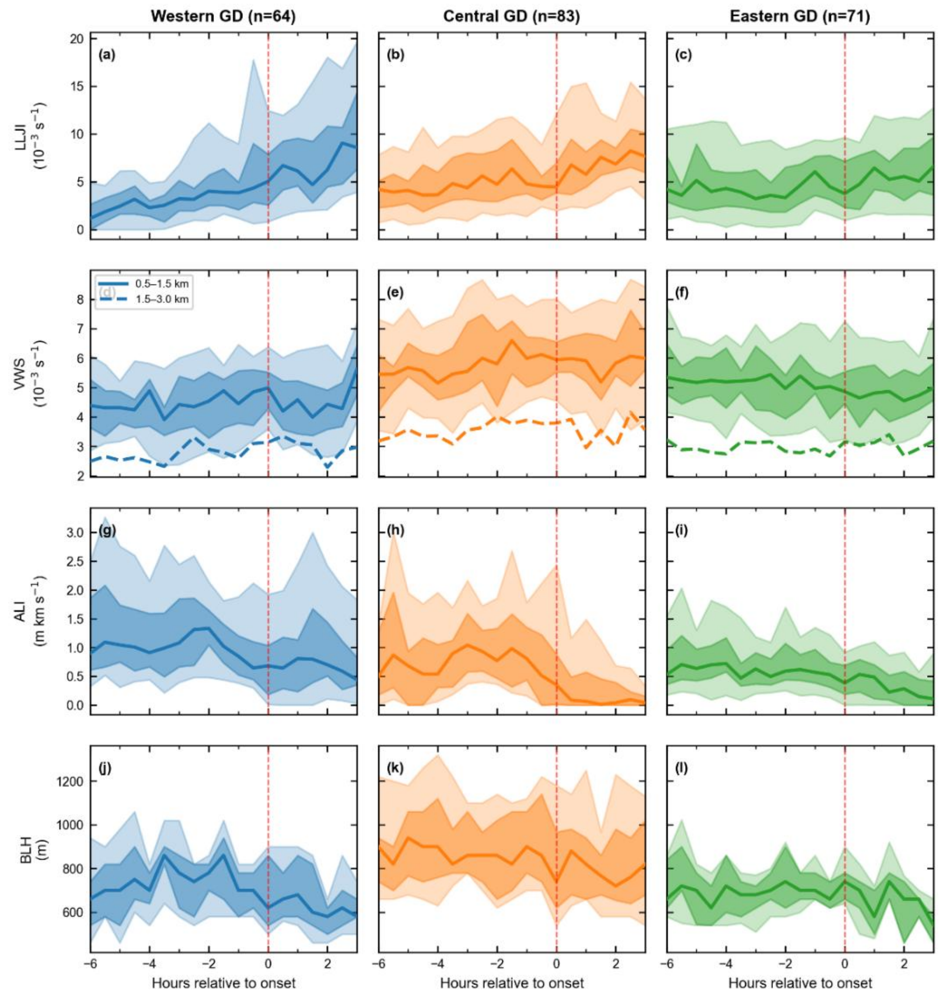

Figure 8: Composite temporal evolution of precursor indices for WSHR events over (a, d, g, j) western GD (n = 64), (b, e, h, k) central GD (n = 83), and (c, f, i, l) eastern GD (n = 71): (a–c) LLJI, (d–f) VWS at 0.5–1.5 km (solid) and 1.5–3.0 km (dashed), (g–i) ALI, and (j–l) BLH. Lines show medians; dark shading shows the bootstrap 95 % CI of the median; light shading shows the interquartile range. The red dashed line marks onset (t = 0).

The VWS (solid line in Fig. 8d–f) at 0.5–1.5 km exceeded the values at 1.5–3.0 km (dashed line) in all regions and at all times, reflecting the strong wind speed gradient between the surface layer and the jet core. The highest VWS was recorded in central GD (median value approximately 5.5–6.0 × 10^{-3} s^{-1}). Neither layer showed systematic variation in the 1–2 hours preceding precipitation. The ALI (Fig. 8g–i) was intermittent, with intermittent pulses but no sustained accumulation in western and central GD; it remained low and flat in eastern GD. BLH (Fig. 8j–l) showed a weak pattern of initial rise followed by decline in all regions—most pronounced in central GD. For example, in central GD, the median value reached approximately 800–850 m near t = −3 h, then dropped to approximately 700 m at the onset of precipitation. However, the bootstrap confidence interval was wide, and the signal was indistinguishable from the sampling variability at the 95% level. A notable feature of

Fig. 8 is the large IQR relative to the temporal changes of the medians, reflecting the diversity of synoptic settings, onset times, and rainfall intensities among WSHR events. Stratified analyses addressing this heterogeneity are presented in Sect. 4.4. Whether pre-onset index values are associated with subsequent rainfall intensity is examined in Sect. 4.3.

4.3 Association between precursor indices and rainfall intensity

To assess whether the pre-precipitation index value is related to the subsequent precipitation intensity, Spearman rank correlations are computed between each index and the maximum event-accumulated rainfall, defined as the highest event-total precipitation recorded across all AWS within the sub-region during the event period. The pre-onset window is divided into four periods: $t = -6$ to -4 h, $t = -4$ to -2 h, $t = -2$ to -1 h, and $t = -1$ to 0 h. For each event, the index value is averaged over each period, and the correlation with rainfall intensity is calculated for all events in a given region. This period-averaging approach reduces the number of independent tests relative to a point-by-point sliding-window analysis, while providing a more robust estimate of the index value at each lead time. Significance is assessed at 95 % level ($p < 0.05$).

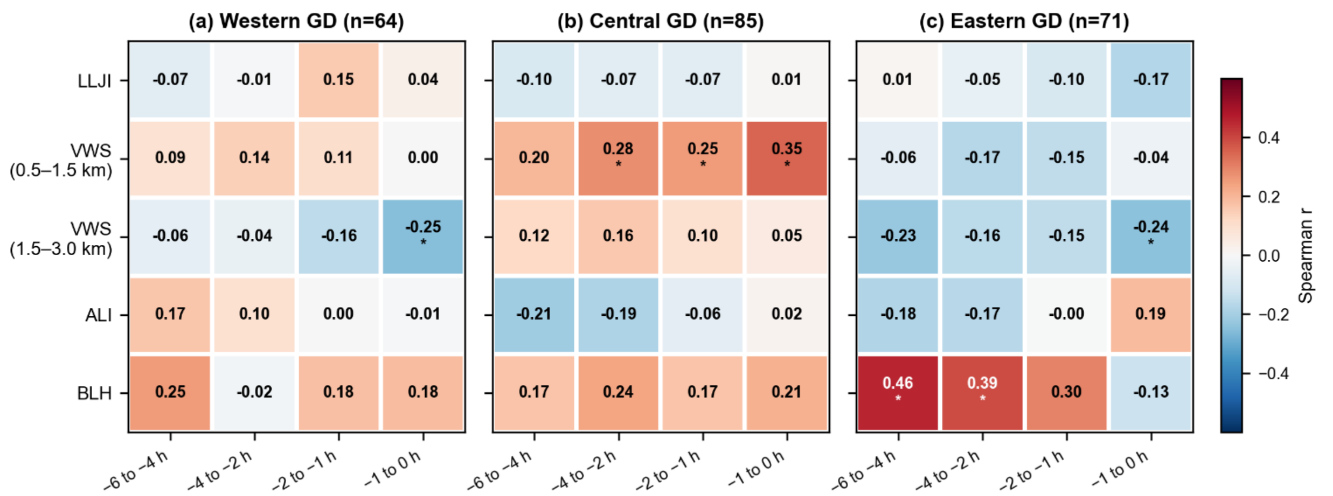

Figure 9: Spearman rank correlations between pre-onset index values (averaged over time) and maximum accumulated rainfall for (a) western GD ($n = 64$), (b) central GD ($n = 85$), and (c) eastern GD ($n = 71$). Correlations are computed over four pre-onset periods. The color shading indicates the correlation coefficient (red: positive; blue: negative). Asterisks denote significance at 95 % level ($p < 0.05$).

The results are summarized in Fig. 9. In central GD (Fig. 9b), VWS at 0.5 to 1.5 km is significantly correlated with rainfall intensity in three consecutive periods ($r = 0.28$ at $t = -4$ to -2 h; $r = 0.25$ at $t = -2$ to -1 h; $r = 0.35$ at $t = -1$ to 0 h ; all $p <$ 0.05), the correlation strengthening toward onset. This sustained positive correlation indicates that stronger low-level shear over the PRD is associated with more intense rainfall.

In eastern GD (Fig. 9c), BLH shows the strongest association with rainfall intensity among all region–index combinations. The correlation is significant in the two earliest periods ($r = 0.46$ at $t = -6$ to -4 h; $r = 0.39$ at $t = -4$ to -2 h; both $p < 0.05$)

but weakens closer to onset. Since eastern WSHR events predominantly occur in the early morning (Sect. 3), when the boundary layer is typically shallow, an anomalously high BLH before onset implies enhanced pre-onset thermodynamic preconditioning of the lower troposphere. The significant correlations at longer lead times suggest that BLH acts as an observational indicator of the pre-convective thermodynamic environment: stronger energy accumulation produces both a deeper boundary layer and, subsequently, more intense rainfall.

Across all three regions, LLJI is not significantly correlated with rainfall intensity during any period. This does not imply that the low-level jet is irrelevant to rainfall: the composite analysis in Sect. 4.2 shows that LLJI increases before onset in western GD, and stratified analysis in Sect. 4.4 confirms that the LLJI is significantly higher for strong-rainfall events. The absence of a linear Spearman correlation suggests that the relationship between LLJI and rainfall intensity may be nonlinear.

In summary, time-dependent correlation analysis identified two robust associations: the 0.5–1.5 km VWS in central GD and precipitation intensity, and the BLH in eastern GD. Both signals persisted over multiple consecutive time periods. While the LLJI is the clearest temporal precursor — showing a marked increase before onset (Sect. 4.2) — it does not serve as a linear intensity predictor, as it shows no significant rank correlation with rainfall amount. This distinction suggests that LLJI may play a nonlinear, threshold-type role in convective triggering rather than scaling proportionally with rainfall intensity. The physical explanation for these regional differences is discussed in Sect. 4.4.

4.4 Physical interpretation of regional differences

Sect. 4.2 and 4.3 have shown that the nature of the precursor signals differs in the three regions: LLJI is the clearest temporal precursor in western GD, VWS at 0.5–1.5 km is the strongest correlate of rainfall intensity in central GD, and BLH shows the strongest intensity association in eastern GD. This section investigates the physical processes underlying these regional contrasts through stratified composites, vertical structure analysis, and ERA5 diagnostics.

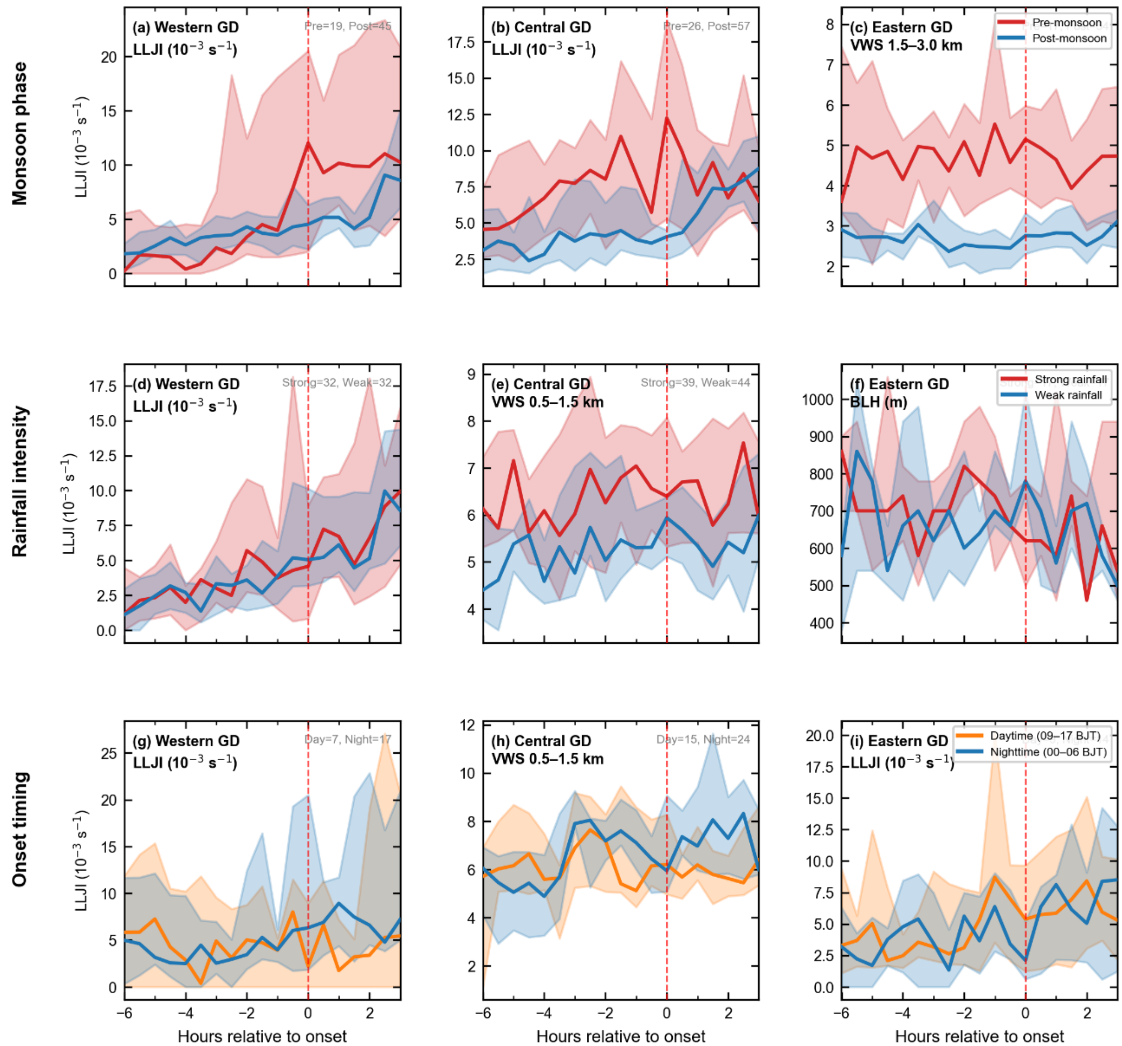

Figure 10: Stratified composite time series of selected precursor indices for the most physically interpretable index–stratification combinations (complete results in Figs. S1–S3). Row 1 (a–c): pre-monsoon (red) versus post-monsoon (blue) for LLJI in western and central GD and VWS at 1.5–3.0 km in eastern GD. Row 2 (d–f): strong-rainfall (red) versus weak-rainfall (blue) events for LLJI in western GD, VWS at 0.5–1.5 km in central GD, and BLH in eastern GD. Row 3 (g–i): daytime versus nighttime onset events, where daytime and nighttime are defined following the onset-hour distributions in Sect. 3, for LLJI in western GD, VWS at 0.5–1.5 km in central GD, and LLJI in eastern GD. Lines show medians; shading shows the bootstrap 95 % CI. Event counts for each group are annotated.

Stratified composites (Fig. 10) show the most significant differences in the selected index-stratified combinations; complete stratification results for all indices and the three stratification methods are shown in Figs. S1–S3. Pre-monsoon events exhibit larger LLJI fluctuations before precipitation than post-monsoon events (Fig. 10a, b). The strongest contrasts emerge when stratified by precipitation intensity (Fig. 10d–f): strong precipitation events in western GD show higher LLJI starting 2 hours before precipitation, strong events in central GD show persistently higher 0.5–1.5 km VWS throughout the entire pre-

precipitation window, and strong events in eastern GD show higher BLH 2 hours before precipitation. Stratification by onset time (Fig. 10g–i), where daytime and nighttime events are defined according to the onset time distribution identified in Sect. 3, indicates that nighttime events in central GD are accompanied by a significantly enhanced 0.5–1.5 km VWS approximately 2 hours before precipitation. These patterns prompt a more in-depth examination of the vertical structure of the low-level jet and its relationship with precipitation intensity.

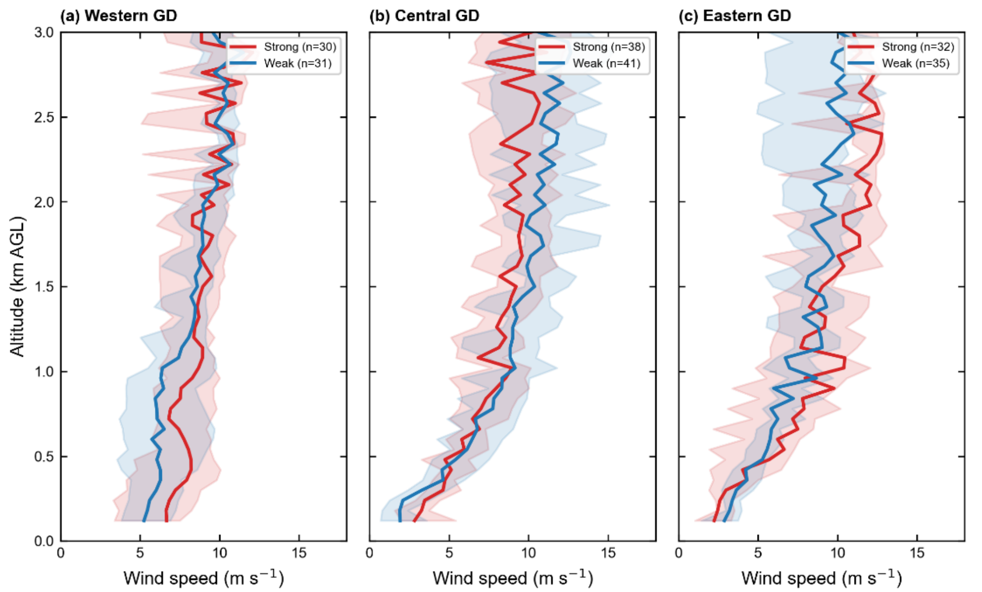

Figure 11: Composite wind speed profiles averaged over *t* = −3 to 0 h for strong-rainfall (red) and weak-rainfall (blue) events in (a) western GD, (b) central GD, and (c) eastern GD. Lines show medians; shading shows the interquartile range.

The composite wind speed profiles of strong and weak precipitation events (Fig. 11) reveal different characteristics of the low-level jet in the three regions. In western GD (Fig. 11a), the strong precipitation group systematically shows higher wind speeds below 1.5 km. In eastern GD (Fig. 11c), the strong precipitation group has a lower jet core height (2.40 km vs. 2.94 km for the weak events) and stronger peak wind speeds (12.8 vs. 11.2 m s^{-1}). In central GD (Fig. 11b), the two groups of strong events show slightly higher wind speeds below 0.5 km, and the precipitation intensity in this region cannot be distinguished solely by the overall structure of the jet.

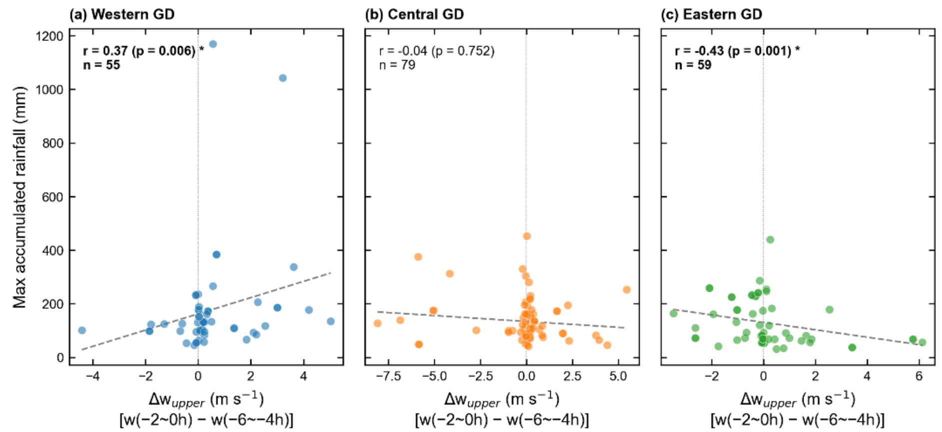

Figure 12: Spearman rank correlation between the upper-level (3–5 km) vertical velocity change (Δw = w at t = −2 to 0 h minus w at t = −6 to −4 h) and maximum accumulated rainfall for (a) western GD, (b) central GD, and (c) eastern GD. A positive Δw indicates strengthening ascent approaching the onset.

A further diagnostic is provided by the change in upper-level (3–5 km) vertical velocity between the baseline period (t = −6 to −4 h) and the near-onset period (t = −2 to 0 h), denoted Δw (Fig. 12). ~~profiles of~~ A positive Δw indicates upward strengthening motion approaching the onset; a negative Δw indicates weakening. The correlation between Δw and rainfall intensity reveals a striking regional contrast. In western GD (Fig. 12a), Δw is positively correlated with rainfall (r = 0.37, p = 0.006): events with strengthening ascent before onset produce heavier rainfall. Moreover, Δw is positively correlated with $\Delta LLJI$ (r = 0.34, p = 0.012; Fig. S4), and this association holds after accounting for synoptic-scale geopotential height trends at 925 and 850 hPa (partial r = 0.27–0.31, p < 0.05; not shown).

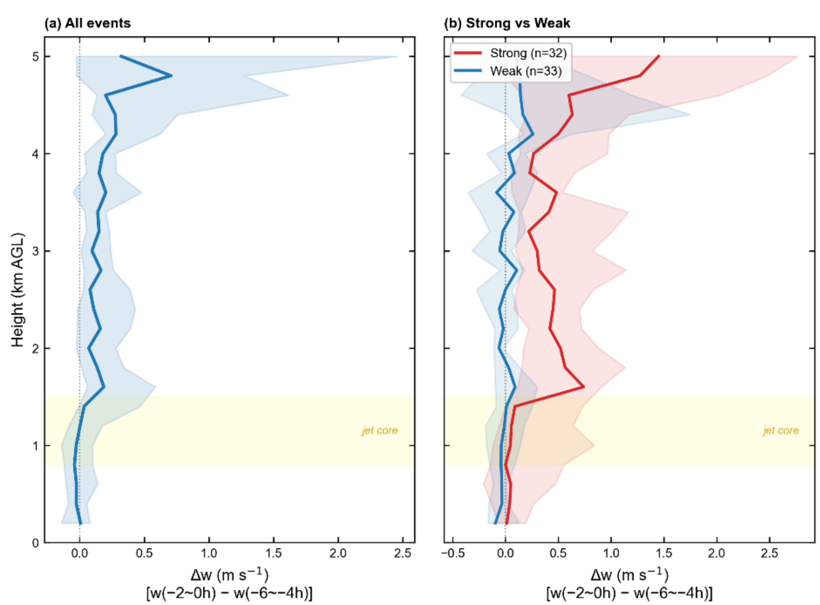

Figure 13: Vertical profiles of the pre-onset vertical velocity change (Δw = mean w at $t = -2$ to 0 h minus mean w at $t = -6$ to -4 h) in western GD. (a) All events: solid line shows the composite median and shading shows the bootstrap 95 % confidence interval. (b) Strong-rainfall (red) and weak-rainfall (blue) events. The yellow band marks the jet core layer (0.8–1.5 km AGL) identified from Fig. 11a.

The vertical structure of Δw is consistent with this: Δw is close to zero in the jet core (0.8–1.5 km) and increases sharply above 1.5 km (Fig. 13), consistent with the upward motion driven by convergence above the jet core. In strong precipitation events, the larger Δw above 1.5 km is more pronounced. Combined with the fact that there is no difference in CAPE between strong and weak events in this region (Fig. 14a, $p = 0.66$), these results support the view that the enhancement of LLJ in western GD directly amplifies the low- to mid-level upward motion, resulting in stronger precipitation.

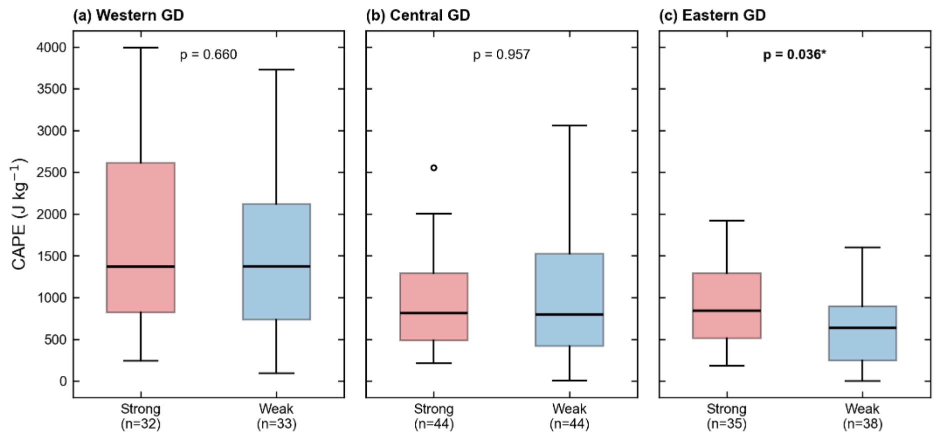

Figure 14: Pre-onset CAPE (ERA5, averaged over $t = -6$ to -2 h) for strong-rainfall (red) and weak-rainfall (blue) events in (a) western GD, (b) central GD, and (c) eastern GD. The box plots show the median, interquartile range, and whiskers extending to 1.5 × IQR. The p value of the Mann-Whitney U-test is annotated; an asterisk denotes $p < 0.05$.

In eastern GD (Fig. 12c), the relationship is reversed: Δw is negatively correlated with precipitation ($r = -0.43$, $p = 0.001$). This decrease in Δw is not driven by changes in the low-level jet stream, as $\Delta LLJI$ and Δw are uncorrelated in this region (Fig. S4, $r = 0.15$, $p = 0.26$), suggesting that the suppression mechanism operates independently of local jet dynamics. The pre-precipitation CAPE of strong precipitation events is significantly higher than that of weak events (Fig. 14c), and the Δw of strong precipitation events is significantly more negative (Fig. S5d). All these indications suggest that the suppression of upward motion in the middle and upper levels prevents the premature release of convective instability, causing instability energy to build up in the lower troposphere; the significantly higher pre-precipitation CAPE and anomalously deep BLH in strong precipitation events are consistent with this accumulation process. ERA5 diagnostics in eastern GD (Fig. S5) showed no significant differences in large-scale 500 hPa vertical velocity ($p = 0.80$) and 925 hPa relative humidity ($p = 0.21$) between strong and weak precipitation events. Only 925 hPa temperature showed a significant difference (median 22.5 vs. 21.8°C; $p = 0.004$), with strong events consistently being warmer. In central GD, neither Δw nor CAPE distinguishes between strong and weak events (Fig. 12b, $p = 0.75$; Fig. 14b, $p = 0.96$). The relationship between $\Delta LLJI$ and ΔVWS is region-dependent (Fig.

S6): in western GD they are significantly anti-correlated ($r = -0.26$, $p = 0.044$), in central GD they are uncorrelated ($r = 0.03$, $p = 0.76$), and in eastern GD they are also uncorrelated ($r = 0.03$, $p = 0.84$). These contrasts indicate that central-GD low-level shear is modulated by surface friction rather than LLJ pulsing, while in western and eastern GD, LLJ pulses accelerate the boundary-layer and lower-free-troposphere winds more uniformly.

The composite IVT fields (Fig. 15) show that central GD lies at the confluence of southwesterly flow from the Indian Ocean and southeasterly flow steered by the western Pacific subtropical high (consistent with the moisture transport climatology of Ning et al., 2023). Within this convergent large-scale environment, the low-level wind shear is strongest in central GD among the three regions (Fig. 7). This shear may partly arise from frictional deceleration of the low-level jet over the PRD surface, which would enhance convergence beneath the jet core. To further characterize the spatial structure of pre-onset boundary-layer VWS enhancement and the associated divergence pattern across the PRD, a multi-event profiler analysis is presented in Sect. 4.5.

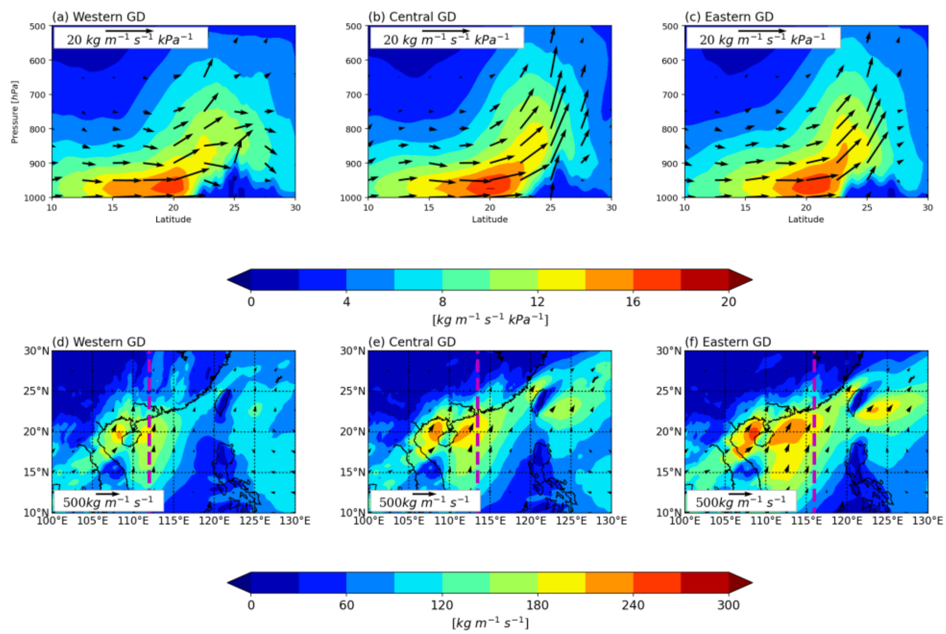

Figure 15: Composite mean moisture transport ~~are characterized by each unintegrated term~~field of WSHR events in ~~Eq (7)~~2016–2020 for ~~diagnosis in horizontal~~the Western (a, d), Central (b, e), and Eastern (c, f) regions. Upper panels (a–c): vertical ~~components for~~ cross-~~section analysis~~ sections of moisture transport ~~and moisture transport diagnosis:~~along the purple lines shown in (d–f); shading shows the horizontal component (kg m^{-1} s^{-1} kPa^{-1}), and arrows show the combined horizontal and vertical components, with the vertical component (VTw) magnified by a factor of 50 for visibility. Lower panels (d–f): spatial distribution of vertically integrated water vapour transport (IVT; kg m^{-1} s^{-1}), with arrows showing IVT vectors and the purple line marking the transect location of the upper panels. IVT is integrated between 1000 and 850 hPa. Fields are averaged over $t = -6$ to -2 h before onset.

$$\cancel{VT_u = \frac{1}{g}\int_{p_b}^{p_t} qu\, dp ,} \qquad \cancel{(10)}$$

$$VT_v = \frac{1}{g}\int_{p_b}^{p_t} qv\,dp\,, \tag{11}$$

$$VT_w = \frac{1}{g}\int_{p_b}^{p_t} qw\,dp\,, \tag{12}$$

$$-m = \frac{\partial q}{\partial t} + \nabla\cdot(VT_u, VT_v) + \frac{\partial \omega q}{\partial p}\,, \tag{13}$$

~~where $VT_{u/v/w}$ are three components of moisture transport in each vertical layer in kg m^{-1} s^{-1}, p_t and p_b are top and bottom layers of each ERA5 vertical layer ($p_t \geq 500$ hPa and $p_b \leqslant 1{,}000$ hPa), w is vertical components of velocity in m s^{-2}. m represents condensation rate at specific grid in three-dimensional space (time, latitude and longitude) related to precipitation rate, which consists of local rate of change of moisture $\frac{\partial q}{\partial t}$, divergence of moisture transport $\nabla\cdot(VT_u, VT_v)$ and vertical moisture transport term $\frac{\partial \omega q}{\partial p}$. Meanwhile, we used Convective Available Potential Energy (CAPE) in ERA5 (unit: J) to study convection.~~

~~3 Overview of WSHR~~

~~We found eight WSHR events from April to July, 2019 in Guangdong Province following the WSHR definitions. Table 1 shows the times of precipitation onset and the maximum hourly precipitation for each of the eight cases (all times are in UTC). Figure 2 shows the distribution of daily precipitation observed by high-density automatic weather stations for each case. Figure 3 shows the daily mean precipitation calculated from all cases. The WSHR is mainly concentrated in three areas: the vicinity of Hailing Island in western Guangdong (hereafter the western region), the Pearl River Delta urban agglomeration area (the central region), and the Chaozhou area in eastern Guangdong (the eastern region). The Pearl River Delta urban agglomeration region experienced the highest cumulative precipitation levels, particularly in the vicinity of the Greater Bay Area.~~

	0413	0418	0420	0526
Start time(UTC)	05:50	09:45	03:30	01:00
Radar stations	HLD	ZH	LG	CZ
Max Rainfall intensity(mm/h)	21.9	9.6	14.5	13.9
Region	Western	Central	Central	Eastern
	0529	0610	0624	0710
Start time(UTC)	18:40	07:35	01:45	21:00
Radar stations	HLD	HD	ZC	CZ
Max rainfall intensity(mm/h)	10.4	10.6	7.9	6.8
Region	Western	Central	Central	Eastern

~~**Table 1: General overview of eight WSHR events.**~~

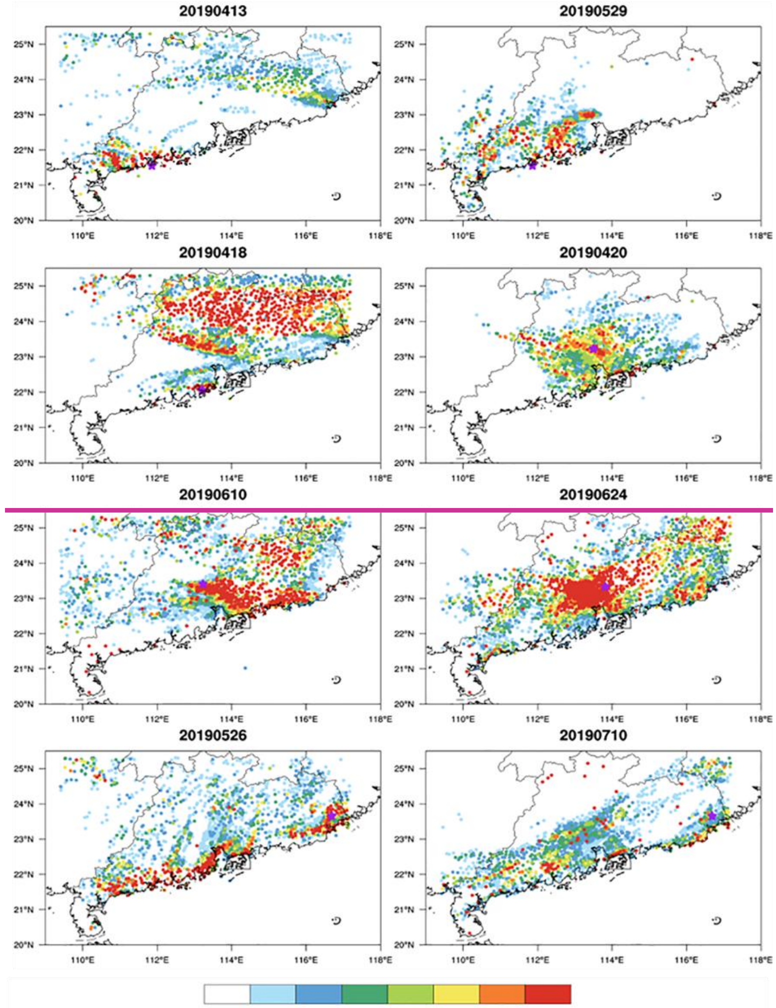

~~**Figure 2: Rainfall distribution of individual WSHR cases in 2019 (unit: mm d^{-1}).**~~

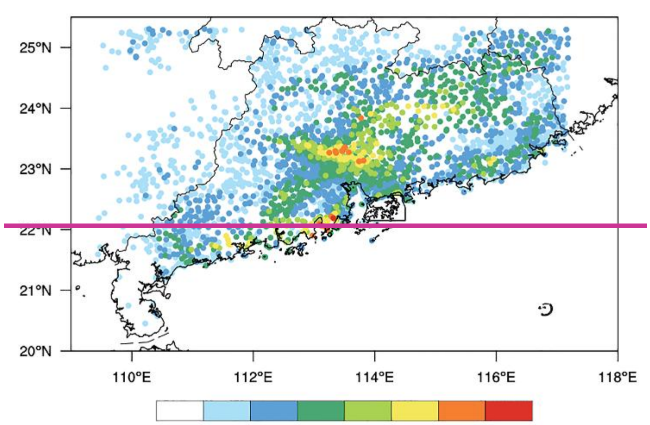

~~**Figure 3: Composite mean of WSHR rainfall amount distribution (unit: mm d^{-1}).**~~

~~Figure 4 and Figure 5 show synoptic conditions at lower levels for each case of the WSHR. Western region events are dominated by high pressure system or without weather systems, with mild southerly wind. The synoptic conditions in the central and eastern regions exhibit significant similarities, characterized by a low-pressure system in northwestern South China, accompanied by the edges of a subtropical high in the eastern areas, as well as the presence of monsoon troughs and convergence zones.. These WSHR events in two regions are dominated by southerly or southwesterly with high wind speed, with jet streams at 850 hPa and 925 hPa. Southerly prevails in South China in April to May, and southwesterly prevails in June to July.~~

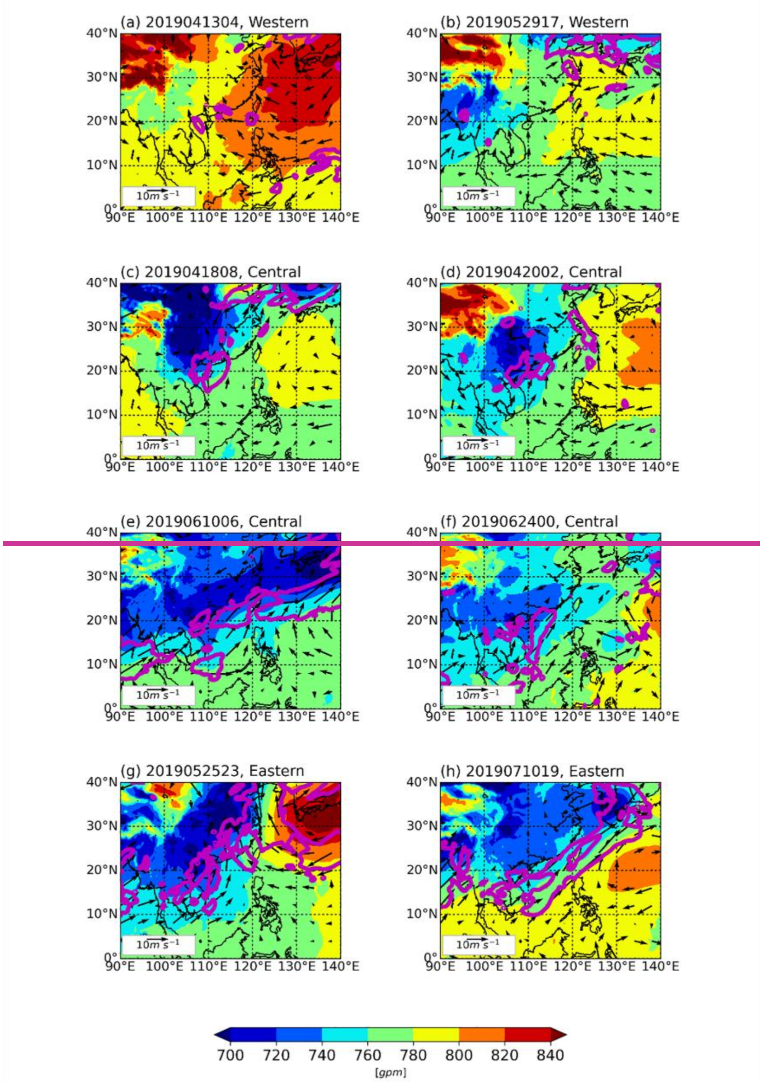

In summary, the regional differences in precursor signals reflect fundamentally different relationships between low-level jets and precipitation intensity. In western GD, LLJ enhancement independent of synoptic-scale forcing promotes mid-to-upper-level upward motion, with a Δw vertical structure consistent with convergence-driven ascent. In eastern GD, pre-precipitation upward motion weakens, accompanied by higher boundary-layer temperatures and associated CAPE accumulation, while large-scale dynamics and low-level moisture conditions show no significant difference between strong and weak events. In central GD, governed by frictional shear modulation, the magnitude of lower-level VWS determines precipitation intensity.

4.5 Multi-event profiler analysis of low-level VWS enhancement in central Guangdong

To verify that the correlation between the lower-level VWS and precipitation intensity in central GD in Fig. 9 reflects a boundary-layer signal rather than a byproduct of synoptic-scale forcing, Spearman partial correlations (Fig. S7) were calculated after controlling for the mean ERA5 geopotential height (Z850 and Z925) in central GD. The 0.5–1.5 km VWS remained significantly correlated with precipitation in the P2–P4 windows, while the 1.5–3.0 km control layer showed no significant correlation in any window, confirming that the signal is confined to the boundary layer.

To examine the spatial structure of pre-onset VWS enhancement, per-station anomaly composites at 0.5–1.5 km were computed by subtracting each profiler's onset-hour-matched background median from the 3-h pre-onset mean (Fig. 16). All seven stations showed positive median anomalies, confirming that VWS enhancement is a widespread feature across central GD. The largest median anomaly (+1.81 m s^{-1} km^{-1}) was observed at Luogang (LG), located within the Changling National Trail System, a forested recreation area in eastern Guangzhou, with the lowest 3-km urban fraction (22 %, LCZ 1–10) among all seven stations. This is consistent with the VWS enhancement at LG arising from the frictional environment of the surrounding urban agglomeration through which the southerly inflow has passed, rather than from the local surface beneath the profiler. Three other stations located well within the PRD urban agglomeration — Huadu (HD), Conghua (CH), and Shenzhen (SZ) — also showed sizeable positive anomalies. Stratifying events by hourly peak rainfall (median split at 71 mm h^{-1}), six of seven stations showed larger anomalies during strong precipitation events, consistent with the VWS–rainfall relationship documented in Fig. 9.

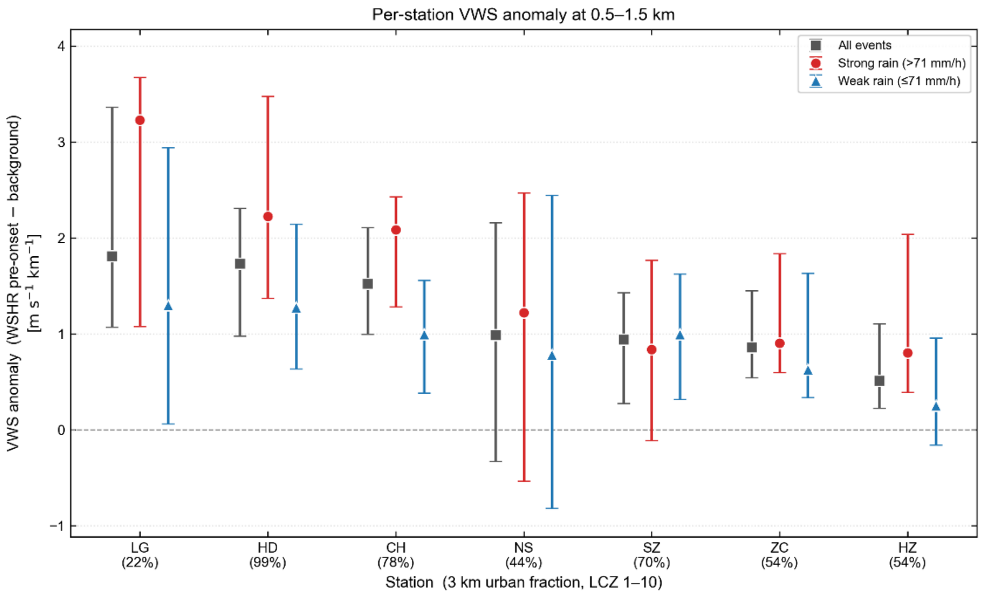

Figure 16: Per-station VWS anomaly composites at 0.5–1.5 km (3-h pre-onset mean) for the seven wind profiler stations in central GD, based on WSHR events during 2016–2020. Stations are ordered by the all-events median (grey squares); error bars denote bootstrap 95 % confidence intervals (*N* = 2000). Red circles and blue triangles show medians for events with hourly peak rainfall above and below the 71 mm h^{-1} split, respectively. x-axis labels include each station's 3-km urban fraction. Station codes: NS (Nansha), LG (Luogang), HD (Huadu), CH (Conghua), ZC (Zengcheng), SZ (Shenzhen), HZ (Huizhou Longmen).

The wind speed anomaly profiles along the dominant southerly inflow path (Fig. 17a; station and triangle locations shown in Fig. S9) show that WSHR events enhance the low-level flow at the coastal station NS by approximately +2.4 m s^{-1} in the lowest 0.5 km, but this enhancement is progressively attenuated inland — to roughly +0.8 m s^{-1} at LG and near zero at HD. At heights above ~1 km, the three stations show comparable enhancement. Such spatially non-uniform deceleration within the boundary layer implies, by mass continuity, enhanced convergence where the inflow decelerates rapidly and relative divergence where it remains strong. The absolute divergence composites (Fig. S8) show that the four Bellamy triangles already possess a strong climatological gradient: the background median divergence ranges from +2.5 × 10^{-5} s^{-1} (divergent) at LG–CH–ZC to −2.5 × 10^{-5} s^{-1} (convergent) at LG–HD–CH, indicating that the northern triangle is climatologically convergent due to its location in the terrain-transition zone north of HD. Against this baseline, WSHR events impose an additional south-to-north divergence anomaly dipole (Fig. 17b). At 1.15 km, the four triangles trace a monotonic gradient: from +2.2 × 10^{-5} s^{-1} (divergence enhancement) at the southern coastal triangle NS–ZC–SZ, through −1.5 × 10^{-5} s^{-1} at NS–LG–ZC and −2.6 × 10^{-5} s^{-1} at LG–CH–ZC, to −3.8 × 10^{-5} s^{-1} (convergence enhancement) at LG–HD–CH. This dipole is vertically confined to below ~1.5 km, matching the layer of spatially non-uniform deceleration in Fig. 17a, and its convergent northern branch provides a favorable dynamical environment for convective initiation during WSHR events. HD itself combines a 99 % 3-km urban fraction with an immediate transition to higher terrain to the north, and whether the climatological convergence is controlled primarily by the urban surface, the orographic discontinuity, or their interaction cannot be determined from the present profiler network. The spatially non-uniform deceleration diagnosed in Fig. 17a may arise from a combination of urban roughness, orographic forcing, and land–sea contrast; disentangling these contributions is beyond the scope of the present observational study and requires future numerical sensitivity experiments.

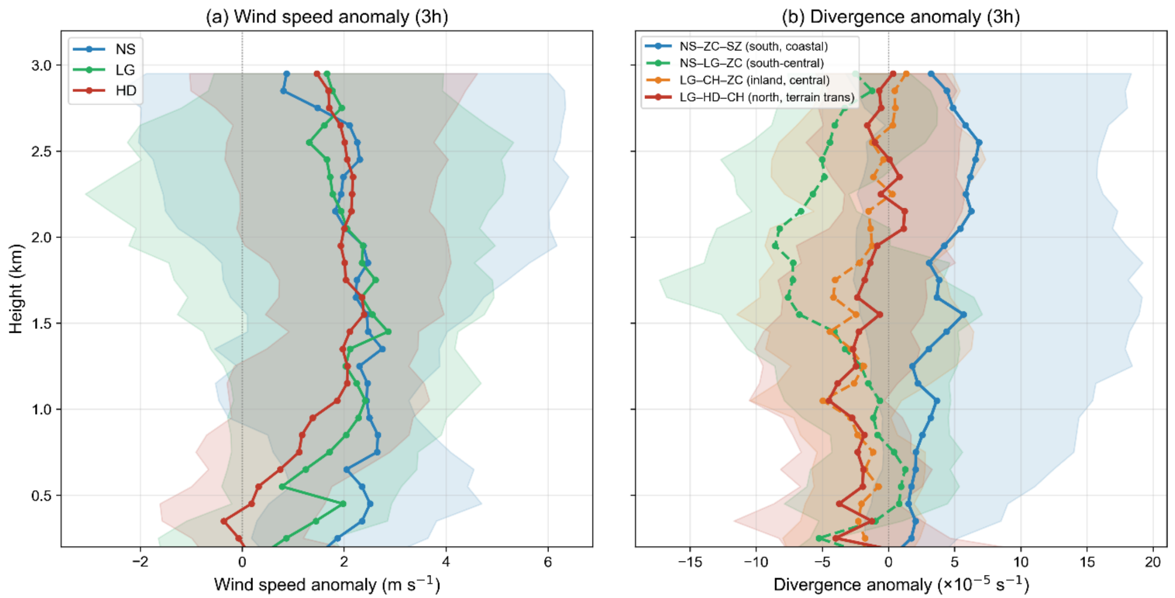

Figure 17: Boundary-layer anomaly composites for WSHR events in central GD, averaged over the 3 h preceding rainfall onset. Anomalies are defined as the event composite minus the onset-hour-matched background median. (a) Wind speed anomaly profiles at NS, LG, and HD. (b) Divergence anomaly profiles for four Bellamy triangles, arranged from south to north by centroid latitude: NS–ZC–SZ, NS–LG–ZC, LG–CH–ZC, and LG–HD–CH. Solid lines show composite medians and shaded bands show interquartile ranges. Triangle geometry is shown in Fig. S9.

5 Conclusions and Discussion

5.1 Summary

This study investigates the precursor signals of WSHR over Guangdong Province using WPR observations of 226 events during 2016–2020 across three subregions: western, central, and eastern GD. Five profiler-derived indices—LLJI, VWS at 0.5 to 1.5 km and 1.5 to 3.0 km, ALI, and BLH—are analysed through composite time series, period-based rank correlations, stratified composites, and ERA5-based thermodynamic diagnostics.

Among the five indices, LLJI exhibits the clearest temporal evolution before onset, roughly doubling its baseline value in western GD with the increase concentrated in the final 1–2 h before rainfall. However, this temporal trend is not statistically robust in central and eastern GD. LLJI does not show a significant rank correlation with rainfall intensity in any region; however, the stratified analysis confirms that strong-rainfall events are characterised by systematically higher overall LLJI levels than weak-rainfall events. VWS at 0.5 to 1.5 km maintains a significant positive correlation with rainfall intensity across three consecutive pre-onset periods in central GD, making it the most persistent intensity predictor in that region. In eastern GD, BLH shows the strongest association with rainfall intensity among all region–index combinations, with the correlation most pronounced in the early pre-onset window ($t = -6$ to -4 h); strong-rainfall events are also characterized by significantly higher pre-onset CAPE than weak-rainfall events. ALI displays episodic pulses rather than a sustained trend, and does not show consistent predictive value in any region.

The analysis of the pre-onset changes in upper-level (3–5 km) vertical velocity (Δw) reveals a fundamental contrast in the rainfall-producing mechanisms between regions. In western GD, Δw is positively correlated with rainfall intensity and with the concurrent change in LLJI, the $\Delta w - \Delta LLJI$ correlation holds after accounting for synoptic-scale geopotential height trends, and the Δw vertical structure is consistent with low-level convergence forcing upper-level ascent. In eastern GD, the relationship is reversed: weakening of the upper-level ascent before the onset is associated with stronger rainfall. This suppression is independent of both local LLJ changes and large-scale subsidence. Strong precipitation events exhibit significantly higher 925 hPa temperatures, and boundary-layer warming drives the CAPE accumulation and boundary-layer deepening observed in strong events. In central GD, neither Δw nor CAPE distinguishes between strong and weak events; instead, the 0.5–1.5 km VWS serves as the primary modulator of precipitation intensity. The LLJI and VWS are temporally decoupled in this region. Multi-event profiler composites show that the WSHR-enhanced southerly inflow undergoes spatially non-uniform frictional deceleration as it crosses the PRD, producing a south-to-north divergence anomaly dipole with convergence enhancement concentrated in the northern PRD (Sect. 4.5).

Among the five indices, three emerge as regionally dominant precursors: LLJI in western GD, VWS at 0.5–1.5 km in central GD, and BLH in eastern GD. These results provide an observational basis for developing region-specific nowcasting guidance: LLJI temporal changes for western GD, VWS at 0.5–1.5 km for central GD, and BLH combined with low-level temperature for eastern GD.

5.2 Comparison with previous studies

The three rainfall processes identified here are broadly consistent with, but extend, previous findings on WSHR mechanisms. Pulsed LLJ intensification in western GD is in agreement with BLJ–terrain interaction and orographic lifting mechanisms widely documented in coastal South China (Liang and Gao, 2021; Pu et al., 2022; Zhang et al., 2022b). The frictional deceleration effect documented across central GD events supports the findings of Gao et al. (2021) and Huang et al. (2019), who attributed convective initiation in Guangzhou to the urban heat island and enhanced convergence. Furthermore, convective maintenance in this urban agglomeration is often aided by evaporative cooling and cold pool outflows from upstream precipitation (Wang et al., 2014), though our current analysis highlights the primary triggering role of friction-induced VWS rather than thermal or cold-pool forcing alone. Regarding eastern GD, our finding of an energy-accumulation process linked to boundary layer warming rather than large-scale moisture transport or subsidence complements and qualifies the previous emphasis on large-scale moisture transport and spatial configurations. Past studies have demonstrated that robust moisture transport from the South China Sea to the Shanwei coast is crucial for triggering warm-sector rainstorms in the eastern region (Ning et al., 2023; Wang et al., 2025; Zhong and Chen, 2017).

This study uses profiler-observed vertical velocity changes to differentiate between direct dynamical forcing and energy-accumulation mechanisms. Previous studies have generally treated BLJ as a uniform triggering factor (e.g., Sun et al., 2019; Zhang and Meng, 2019), while the opposing signs of the Δw–rainfall correlation in western and eastern GD demonstrate that the role of LLJ varies qualitatively in the region. WPR, with its approximately 6-minute temporal resolution and continuous vertical sampling from the surface to 5 to 6 km, is well suited to resolving these pre-onset signals that are not captured by twice-daily radiosondes or hourly reanalysis fields.

5.3 Limitations and future work

This study has several limitations. First, while the 14-station wind profiler network provides high temporal and vertical resolution, its spatial sampling is limited. Observations are lacking on the windward slopes of the Yunwu and Lianhua Mountains, in the central urban area of Guangzhou, and in the gaps between profiler stations, precluding a complete characterization of inflow evolution from ocean to inland. Second, the five-year record (2016–2020) yields limited sample sizes (65–88 events) in each sub-region, which constrains the statistical power of stratified analyses and may not capture the full range of interannual variability in large-scale forcing. Third, as discussed in Sect. 4.5, the observational approach cannot separate the individual contributions of urban roughness, orographic forcing, and land–sea contrast to frictional deceleration and convergence enhancement in central GD; the relative importance of these factors remains unquantified.

Several directions for future work emerge from these findings. High-resolution numerical sensitivity experiments — systematically removing or modifying urban land use, terrain, and coastline geometry — are needed to disentangle the respective contributions to boundary-layer convergence over the PRD. The suppression mechanism that allows CAPE to accumulate before precipitation in eastern GD requires verification with independent thermodynamic profiling to confirm the boundary-layer warming signal beyond ERA5 diagnostics. Finally, translating the regionally distinct precursor signals identified here into operational nowcasting algorithms — for example, real-time monitoring of LLJI trends in western GD, 0.5–1.5 km VWS in central GD, and BLH combined with low-level temperature in eastern GD — represents a natural next step, though the practical skill of such guidance needs to be evaluated through independent case testing and probabilistic verification.

~~**4: Synoptic scale analysis of eight WSHR events at 850 hPa. (a–b) WSHR events in the western region; (c–f) central region and (g–h) eastern region. Geopotential heights in gpm, wind vectors (black arrows) in m s^{-1} with wind speed over 10 m s^{-1} marked in magenta contours.**~~

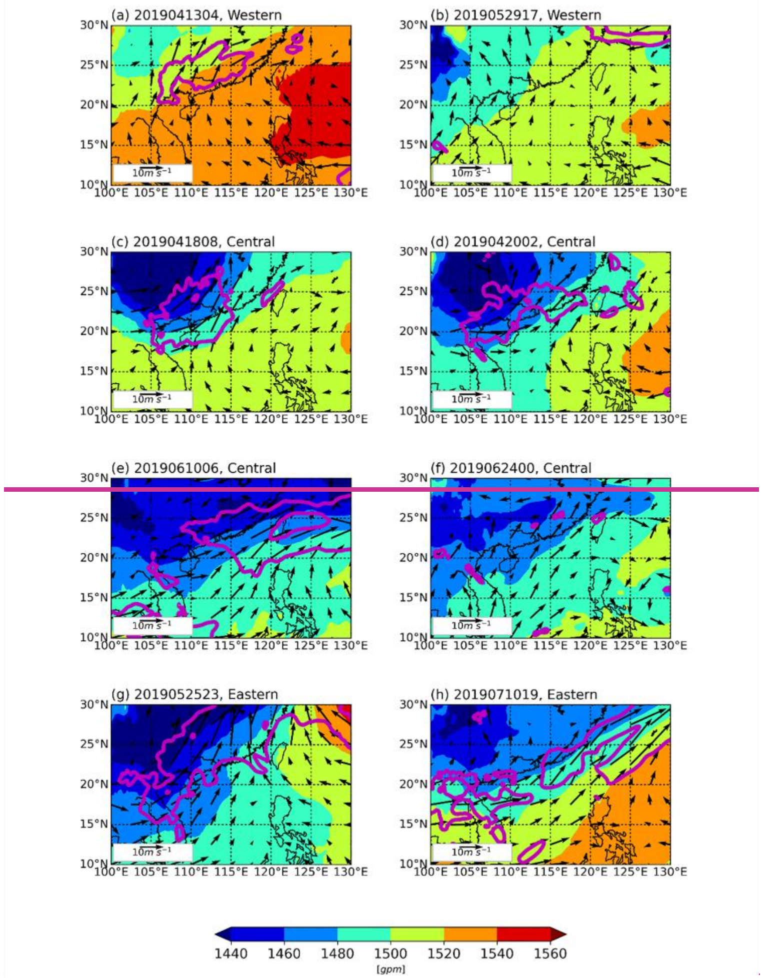

~~**Figure 5: Same as Figure 4, but at 925 hPa.**~~

~~Figure 6 shows time-altitude diagram of wind field and vertical motions of each representative station, while Figure 7 shows VWS mean 3 earlier the onset of the WSHR. Substantial vertical motions are observed within the lowest 6 km of altitude, indicating robust convection. Subsidence prevails hours before the onset, while the vertical motions reversed during and after the onset. Vertical profiles in the western region (Figure 6a, b) shows prevailing southerly below 2 km before the onset of WSHR, and westerly at 3 km and above. Clockwise turning of wind direction with height implies the existence of warm advection in the western region. Wind speed above 2 km significantly increases and turns clockwise with increasing height as local convection develops. There is deflection in wind speed below 2 km with the start of precipitation. The VWS increases where wind speed direction changes significantly (Figure 7a, b). There is strong westerly with the maximum wind speed 18 m s^{-1} over Pearl River Delta, whose vertical profile of horizontal wind show that the strongest jet stream is at 4 km before the onset of precipitation. The strongest wind in the jet is 12 m s^{-1} located at 1–2 km. The altitude of jet maximum decrease before the onset of the WSHR, consistent with previous studies (Li et al., 2024). The wind shear diagram shows large VWS values at~~

~~1–2 km and 4 km, implying strong VWS at jet streams. There is sharp decrease in wind speed below 1 km due to larger friction at urban regions. Wind speed and direction wiggle significantly close to the onset of the WSHR events. The LLJ is located below 2 km and wind directions are homogeneous above 1 km before the onset of WSHR events in the eastern region.~~

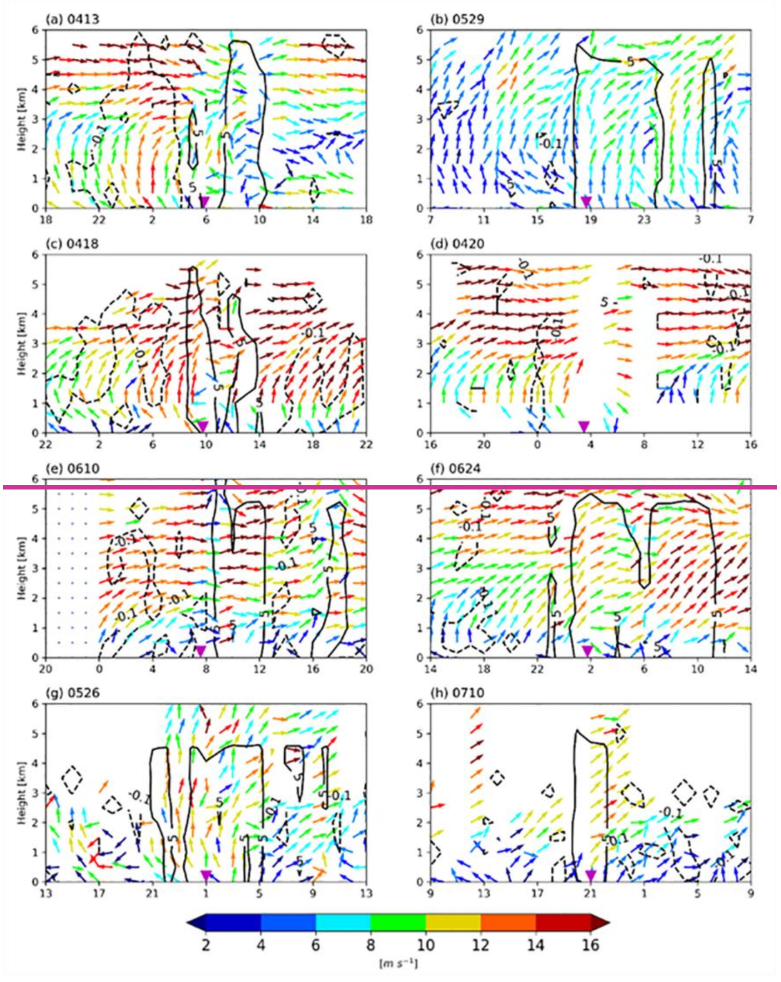

~~**Figure 6: Time-altitude diagrams of horizontal wind for each case. Vectors represent wind speed in m s^{-1}, dashed lines show the contour of -0.1 m s^{-1} of vertical wind speed, the solid shows 5 m s^{-1}, triangles mark the onset of WSHR events.**~~

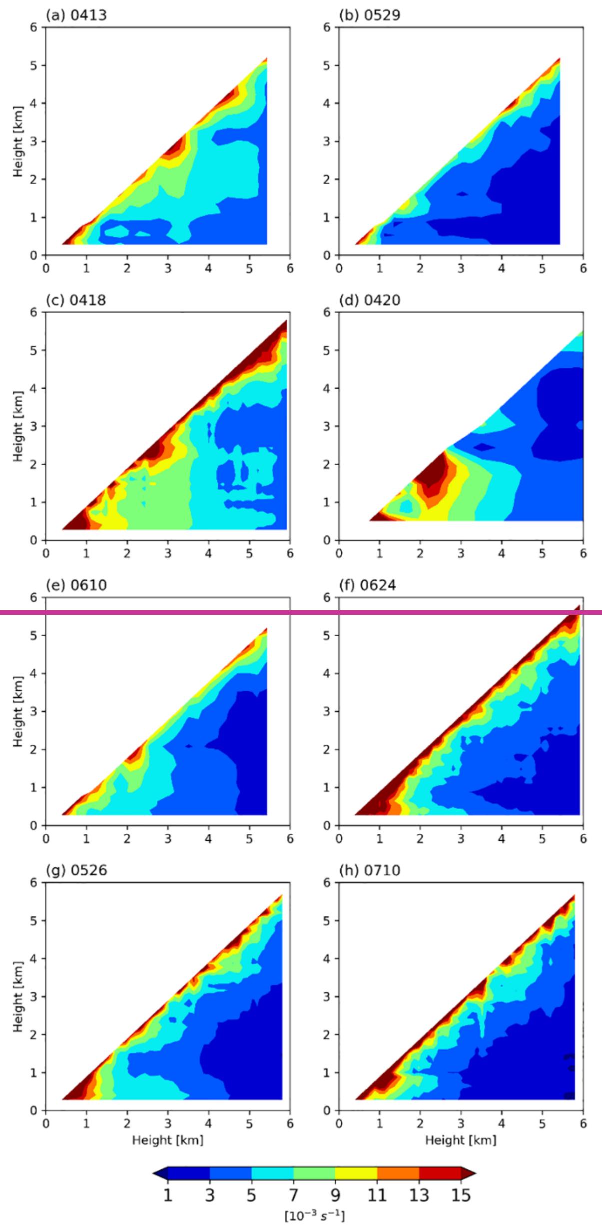

~~**Figure 7: 3-hour mean VWS before the onset of precipitation for each case (unit: 10^{-3} s^{-1}). x axis represents high altitude, y axis represents low altitude.**~~

~~There are significant fluctuations of the horizontal wind speed and direction along vertical dimension through the all cases. The statistical analysis of dynamics prior to the onset of precipitation is conducive to identifying the characteristics of dynamic factors and detecting precursor signals.~~

~~4 Results~~

~~4.1 Indices and Dynamical Calculations~~

~~We standardized the onset of the WSHR events for each case to compute composites of LLJI, VWS, ALI and BLH indices from 12 hours before the onset to 12 hours after the onset (Figure 8). Results show that peak values of LLJI and ALI are observed 4 hours before the precipitation with consistent changes, implying the sudden increased instability into the boundary layer and upper atmosphere, with a sudden change of the wind speed paired with a more intense convection. The VWS attains maximum values within 0–1 km and 2–3 km, as showed in Figure 7 and into Supplementary Figure S1. (supplementary materials). Therefore, we computed the VWS at 0.5–1.5 km and 2–3 km, respectively. Stronger VWS is observed at 0.5–1.5 km, implying significant change in wind speed and direction at 0.5–1.5 km. The BLH first increase and then decrease over the last 4 hours before the onset of the WSHR. The changes of these four indices revealed the atmospheric dynamical processes before the onset of WSHR that atmosphere becomes unstable before the onset of WSHR, that the LLJ strengthens and that the lifting activities are strong. These indices are of great importance to precipitation prediction and analysis.~~

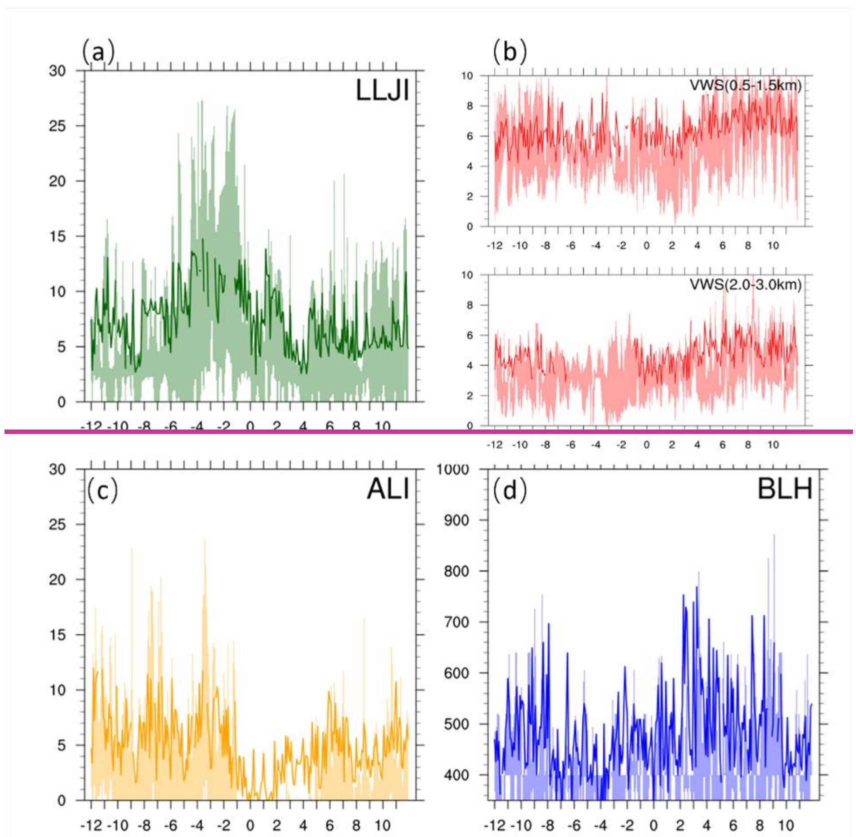

~~Figure 8: Temporal evolutions of (a) LLJI (unit: 10^{-3} s^{-1}), (b) VWS (0.5–1.5km, 2–3km， unit: 10^{-3} s^{-1}), (c)ALI (unit: 10^{-3} m^2 s^{-1}) and (d)BLH (unit: m). x axes are in hours. The onset of the WSHR events is normalized as "0" and the time before the WSHR are labeled as negative numbers. Solid lines represent mean values. Shadows represent 25 %–75 % quantile.~~

~~4.2 Spatiotemporal characteristics of precursor signals~~

~~4.2.1 Summer monsoons over the South China Sea~~

~~Moisture sources of WSHR events are Indian Ocean, western North Pacific and the South China Sea, which affects the spatial distribution of heavy rainfall with varying moisture transport paths . South China is deeply affected by the monsoon system, which is highly associated with moisture transport paths.~~

~~The 2019 South China Sea monsoon broke out in the 2nd pentad in May (National Climate Centre (NCC, http://www.ncc-cma.net), and precipitation is mainly concentrated in the Pearl River Delta (PRD) region and the west coast of Guangdong before the monsoon onset, while the frequency of precipitation in eastern Guangdong increased significantly after the monsoon onset over the South China Sea. When comparing the cases in Yangjiang during pre-monsoon and post-monsoon period (Figure 9), there are distinct variations of the BLH before heavy precipitation events, regardless of the monsoon phase. Results show that LLJI, WVS and ALI are higher than that before the monsoon onset, with sharp decrease in WVS at 0.5–1.5 km. The pre-monsoon cases (blue line) show lower mean BLH with larger oscillation amplitudes, whereas the post-monsoon cases (red line) show higher mean BLH with reduced variability, which is likely due to instability of atmosphere before the monsoon onset and stark contrast of wind fields at different heights. Moreover, consistent wind field at different heights during post-monsoon period and persistent warm, moisture transport are also the reasons why post-monsoon cases show higher mean BLH. Four indices show that there is significant difference in atmospheric conditions to form heavy rainfall between pre-monsoon and post-monsoon season over the western coastal regions.~~

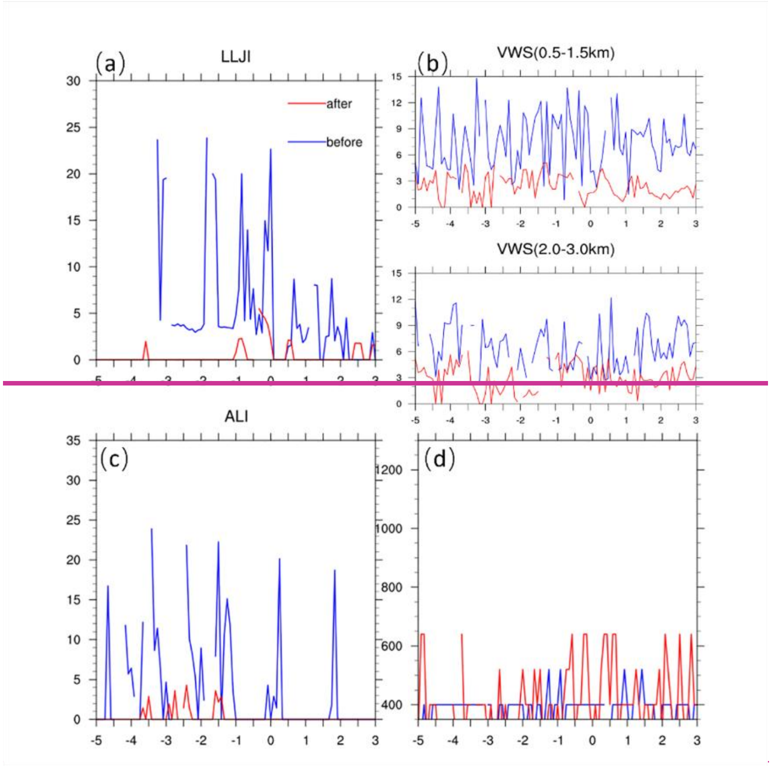

~~Figure 9: Temporal evolution of (a) LLJI (unit: 10^{-3} s $^{-1}$), (b)VWS (0.5-1.5km, 2-3km， unit: 10^{-3} s $^{-1}$), (c)ALI(unit: 10^{-3} m ^{2} s $^{-1}$), (d)BLH (unit: m) before (red) and after (blue) the monsoon onset. X axis represents hours away from the onset of the WSHR events (marked as "0"). The time before the onset is marked as negative numbers.~~

~~The composite mean IVT below 850 hPa 2 hours before the onset of WSHR and equivalent potential temperature are shown in Figure 10. Moisture is mainly distributed over northern South China Sea and coastal regions in Guangdong Province before monsoon onset, where southwesterly from Indian Ocean and southeasterly under the effect of the subtropical high converge, resulting in large LLJI, VWS and ALI over the western region. Monsoon onset results in increase of moisture from the Bay of Bengal and western Pacific Ocean, the retreat of the subtropical high and the northward shift of the LLJ, which fosters moisture transport to reach deep inland. There is increase in the WSHR events over the eastern region after the monsoon onset. There are no dominating weather systems over the western region with weak dynamical effects, but with higher BLH after monsoon onset due to increased sea surface temperature. Overall, the fluctuations and trends of indices are more complex before monsoon onset, implying interactions of multiple atmospheric conditions under unstable atmosphere, resulting in torrential rainfall. The LLJ shifts northward with steady southwesterly after monsoon onset, when the precipitation area and mechanisms are quite different from that before monsoon onset.~~

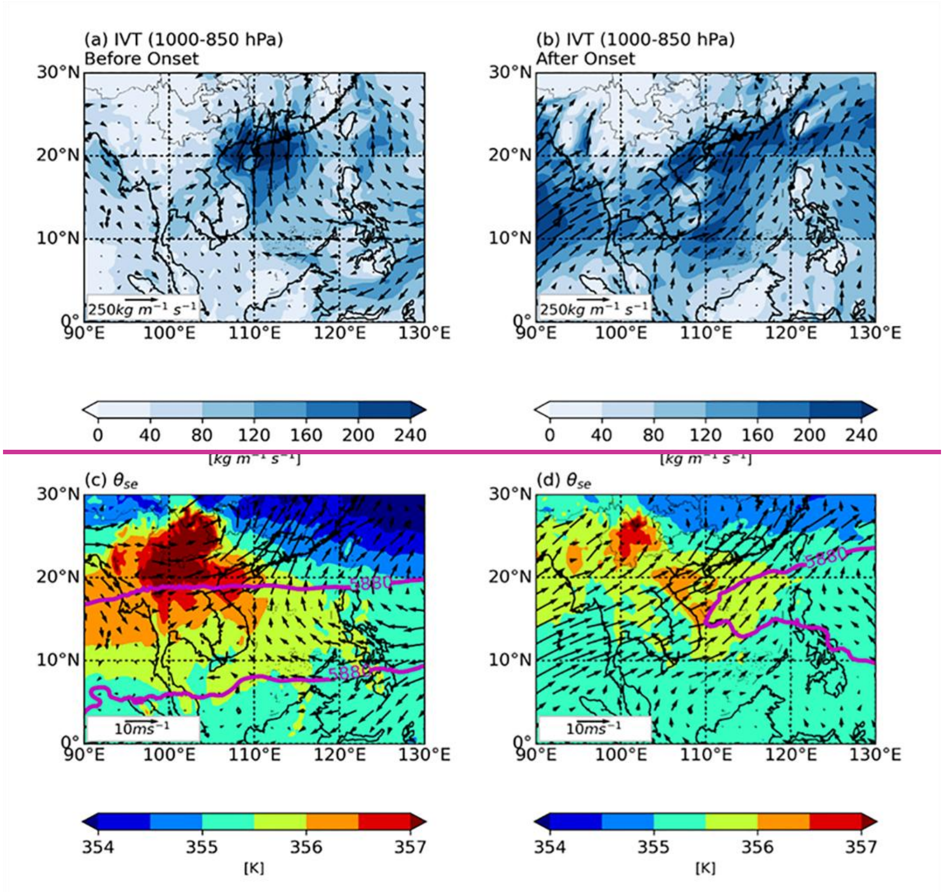

~~**Figure 10: (a, b) the IVT from 1000 hPa to 850 hPa (unit: kg m^{-1} s^{-1}); (c, d) equivalent potential temperature (unit: K) (a, b) before and (c, d) after the monsoon onset.**~~

~~4.2.2 Geographical conditions~~

~~The composite mean time series of LLJI, VWS, ALI and BLH before and after the onset of WSHR events are shown in Figure 11. Discontinuous peak values of LLJI are observed 3 hours before the onset of WSHR events. Initially, the LLJI over the central region exhibits an increase followed by a decrease three hours prior to the onset of WSHR events. This increase-decrease pattern constitutes a significant feature for precipitation nowcasting. During the same period, the LLJI remains considerable over the eastern region, indicating the persistence of the LLJ.. VWS values are about the same at 0.5–1 km and 2–3 km 3 hours before the onset, but with significant decrease in WVS 2 hours before the onset. Large VWS values are observed at 0.5–1.5 km over central regions, implying the effect of surface friction resulting in decreased wind speed at the low level. The increase in ALI is observed over western and central regions 3 hours before the onset of the WSHR, implying~~

~~strong uplift. Maximum mean BLH values are observed over the central region with most significant change, with peak values 2–3 hours before the onset of the WSHR, which is likely the effects of climatological features, terrain and urbanization.~~

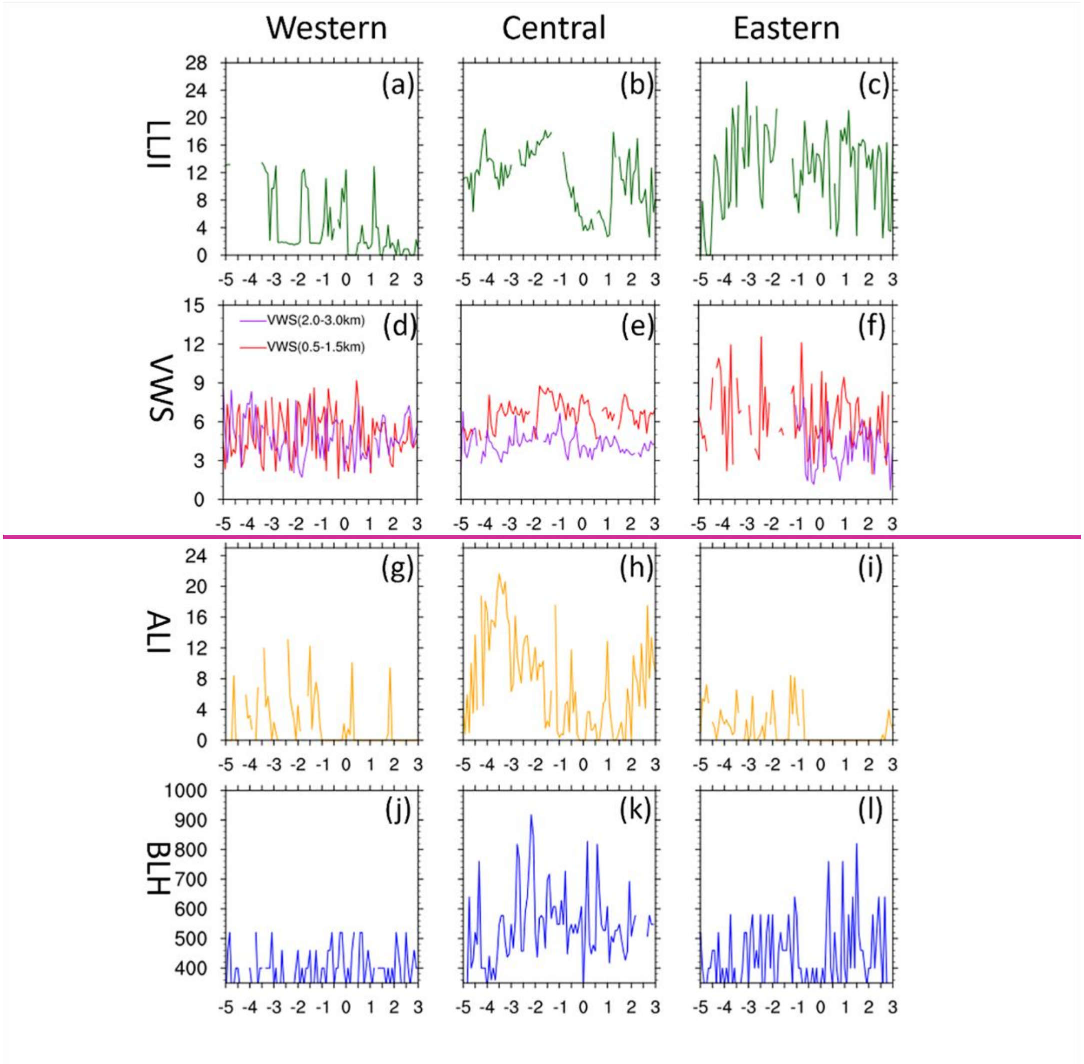

~~**Figure 11: Composite mean temporal evolution of precursor signals of (a–c) LLJI(unit: 10^{-3} s^{-1}), (d–f) VWS (0.5–1.5km, 2–3km, unit: 10^{-3} s^{-1}), (g–i) ALI (unit: 10^{-3} m^{2} s^{-1}) and (j–l) BLH (unit: m) indices over (a,d,g,j) western, (b,e,h,k) central and (c,f,i,l) eastern regions. The onset time is normalized to “0”, before which is labeled as negatives.**~~

~~To investigate the relationship between precursor signals and precipitation in different regions, a sliding window correlation (SWC) analysis is performed (Figure 12). In the western region, significant positive correlations are found between both the ALI and VWS with precipitation during the 2 h period prior to precipitation onset, showing that strong uplift airflow and LLJ are conductive to form precipitation. Within 30–80 minutes prior to the onset, both LLJI and the VWS (2–3 km) are correlated with precipitation, which is likely associated with increase of the LLJ prior to precipitation. The ALI observed 30 minutes~~

~~before the precipitation onset exhibits a positive correlation with precipitation, suggesting that a strong updraft is conducive to precipitation formation. BLH, LLJI and VWS 2–3 hours prior to the onset are positively correlated with precipitation over the central region, implying that higher BLH and stronger LLJ are conductive to heavy rainfall. BLH, ALI, LLJI and VWS at 90 minutes prior to the onset, which is the turning point to trigger the WSHR, are negatively correlated with precipitation. Moreover, convergence of wind speed, weaker VWS, inhibited lifting and lower BLH are observed 90 minutes prior to the onset. In the eastern region, the VWS within 0.5–1.5 km range and the ALI index measured 60–150 minutes prior to the onset of precipitation are significantly positively correlated with precipitation events. In contrast, LLJI exhibits a weaker positive correlation with precipitation. Overseeing the results above, precipitation over western region is sensitive to the ALI and the LLJI 2–3 hours prior to precipitation. The rainfall over central region is sensitive to the strengthening of BLH, LLJI and VWS 2–3 hours prior to the onset and the weakening of the BLH, LLJI and VWS 30–90 minutes prior to the onset. Precipitation over eastern region is sensitive to the increase of ALI and VWS at 0.5–1.5 km, which are 60–150 minutes prior to the onset.~~

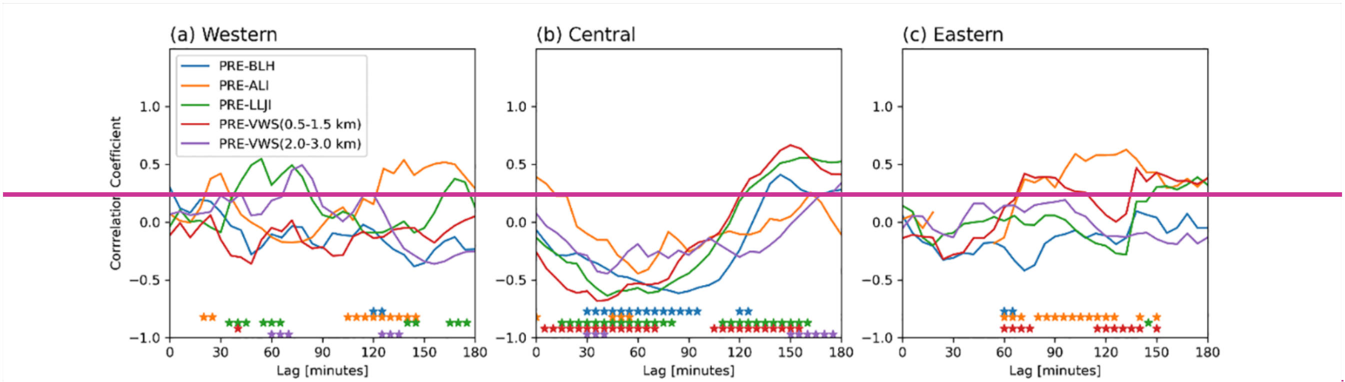

~~**Figure 12. The SWC of precursor signals with precipitation over (a) western, (b) central and (c) eastern region. X axis shows the lag time in minutes. Stars show significance level of 0.05.**~~

~~To further explore the reasons for this inter-regional signal difference, the water vapor fluxes oner the three regions are compared (Figure 13). In the western region, water vapor is mainly concentrated in the lower 900 hPa, and water vapor is mainly transported from south to north and converges. Vertical integration also confirms that the water vapor converges within the region delimited by 20°N–23°N latitudes. This indicates that this region primarily relies on the influx of low-level warm, moist air and may be susceptible to topographic uplift. Water vapor transport in the central region is concentrated at heights of 900 hPa and 700 hPa, which is consistent with the heights of the double LLJs when combined with the heights of the wind profiles in the previous section. The vertical integration results show that the water vapor flux in this region is most concentrated at 23°–25°N. The water vapor flux in the eastern region is more active in the middle layer (500–700 hPa), and the low-level transport is weaker and more extensive compared to the central region. Upward-pointing vector arrows indicate oblique vapor transport through upper-level systems. Vertical integration reveals intense moisture transport across Guangdong~~

~~Province, extending northward. This region exhibits the widest extent and the greatest intensity of moisture transport among the three regions, consistent with regulation by circulation at the edge of the Subtropical High or southwest jet streams.~~

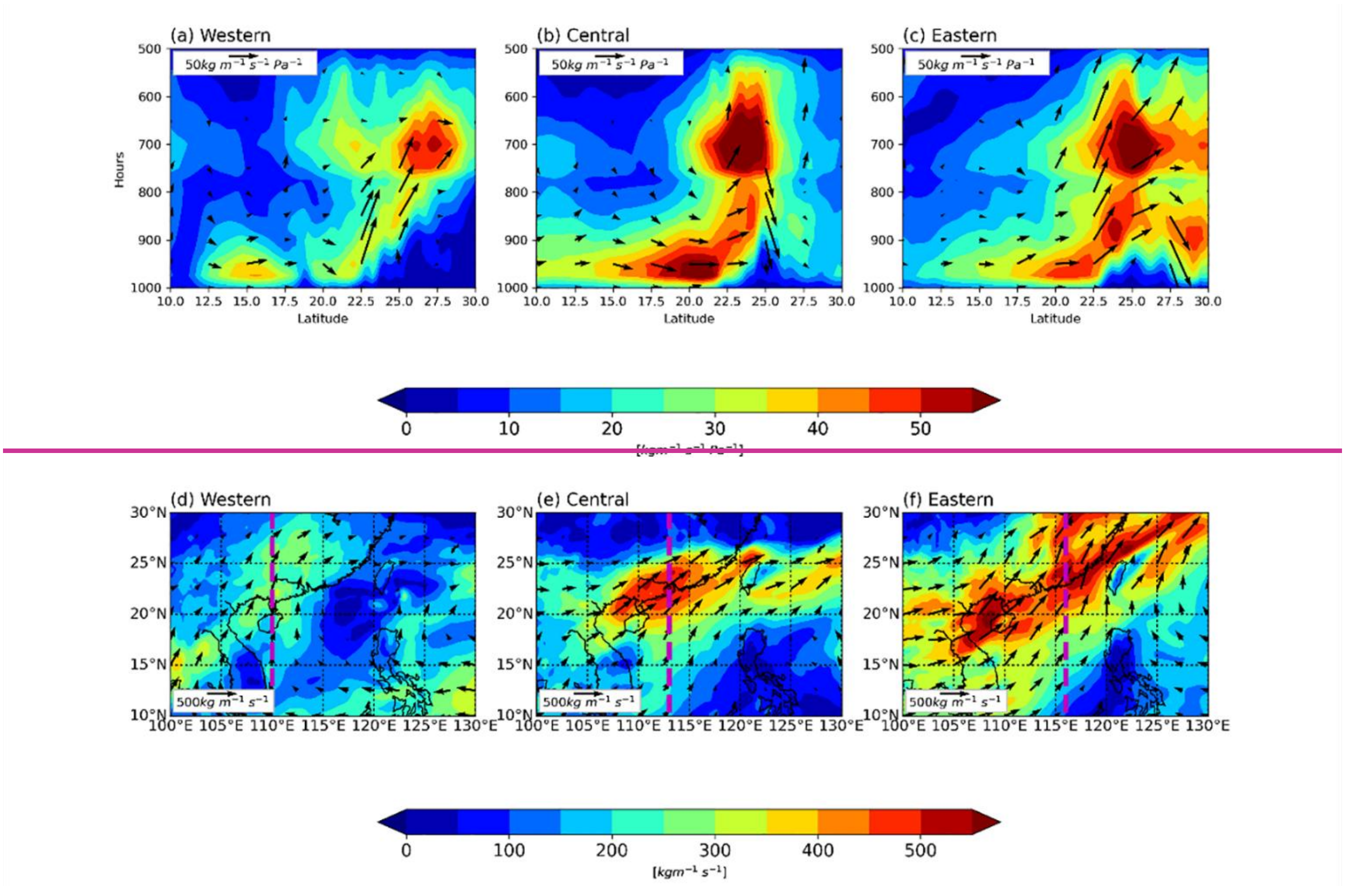

~~**Figure 13. (a) Western region, (b) Central region, (c) Eastern region: Vertical profiles of water vapor flux along the purple line (upper panels) and spatial distribution of vertically integrated water vapor flux (d–f). Arrows represent water vapor vectors. The vertical velocity in the upper panels is magnified by a factor of 50.**~~

~~As shown in figure 14, in order to further clarify the dominant mechanism of WSHR events in the three regions, typical cases in each region are selected and a power term decomposition is performed at the moment of rainfall onset. The water vapor variability in the western region is positive at 500–700 hPa, indicating water vapor accumulation. The water vapor flux divergence is negative at 900–1000 hPa and positive at 600–900 hPa, with strong convergence in the lower layers and divergence in the middle layers. The upward motion is also stronger from the vertical transport term; water vapor in the central region gradually decreases in the 600–900 hPa interval, with strong convergence in the lower layers and strong radiation in the middle layers. In contrast to the western and eastern coastal regions, there is also a convergence zone at 500–700 hPa, which may be related to the coupling of westerly jet and low-level jets. There is a persistent updraft with the largest CAPE~~

~~value, indicating stronger convection; the eastern region has less water vapor variability and is positive overall, which combined with the water vapor integral (Figure 13) shows that there is sufficient water vapor. Low-level convergence is strongest, with a consistent divergence zone at 600–900 hPa, which can lead to stronger vertical pumping.~~

~~In general, it is evident that there are markedly distinct mechanisms among the three regions. In the western region, precipitation is predominantly initiated by orographic lifting effects associated with 900 hPa level moisture advection that occurs perpendicular to the coastlines with short pathways.. Little local moisture over the central region is observed, whose precipitation relies on advective moisture transport in local perspective. Precipitation in the over eastern region mainly relies on moisture transport at 700 hPa under effects of synoptic jet. Paths and height distribution of moisture transport determines the difference of precipitation intensity and spatiotemporal distribution of four indices among three regions.~~

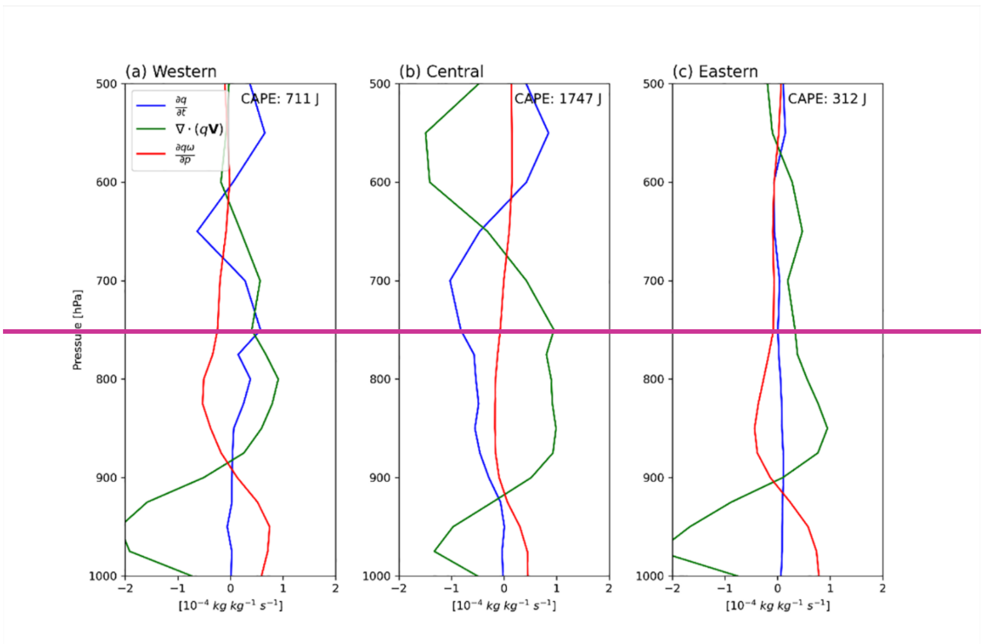

~~Figure 14. (a) Western region, (b) Central region, (c) Eastern region: Regional average vertical profiles of water vapor budget decomposition terms and CAPE values.~~

~~4.3 Typical examples of urban agglomerations~~

~~The precursor signals of WSHR are classified and compared above, and the characteristics of precursor signal changes under different circumstances are counted. The precursor signals of the wind field over the central region are more complex because they are influenced not only by meteorological factors but also by urban agglomerations. To investigate the differential effects of urban versus rural underlying surfaces on wind field characteristics during WSHR events, a typical example in urban~~

~~agglomerations on 20 April 2019 is selected to study the characteristics of wind field changes before the occurrence of WSHR in the Pearl River Delta (PRD) urban agglomerations region. According to Figure 1, Luogang station (59287) is selected as an urban station, and Huadu station (59284), Conghua station (59285) and Zengcheng station (59294) are selected as suburban stations.~~

~~Precursor signals at Luogang station are stronger than the other stations (see Fig. 15), as Luogang station is located in the city center, thereby more affected by urbanization. Compared with the relatively small LLJI in Conghua area, the changing characteristics of LLJI in Zengcheng and Huadu areas are closer. Figure 15b shows the VWS at the four stations, with a weaker signal in Huadu area, which starts to increase 70 minutes before the precipitation onset, 10–15 minutes slower than the other three areas. The ALI of the four stations shows that the updraft in Luogang area starts to increase significantly 100 minutes before the occurrence of precipitation, earlier than the other three sites. The maximum ALI at Luogang is the largest among the four sites, indicating that the vertical motion of the atmosphere is closely related to the subsurface. There are differences in the changes of BLH before the occurrence of precipitation at the four sites. The BLH in Luogang is significantly higher than all the other sites, with sharp increase at 100 min before precipitation, and gradual decrease at 80 min before precipitation. The BLH in Huadu, Conghua and Zengcheng started to increase 75 min before precipitation, later that in Luogang. The change of BLH in Zengcheng area is the least obvious.~~

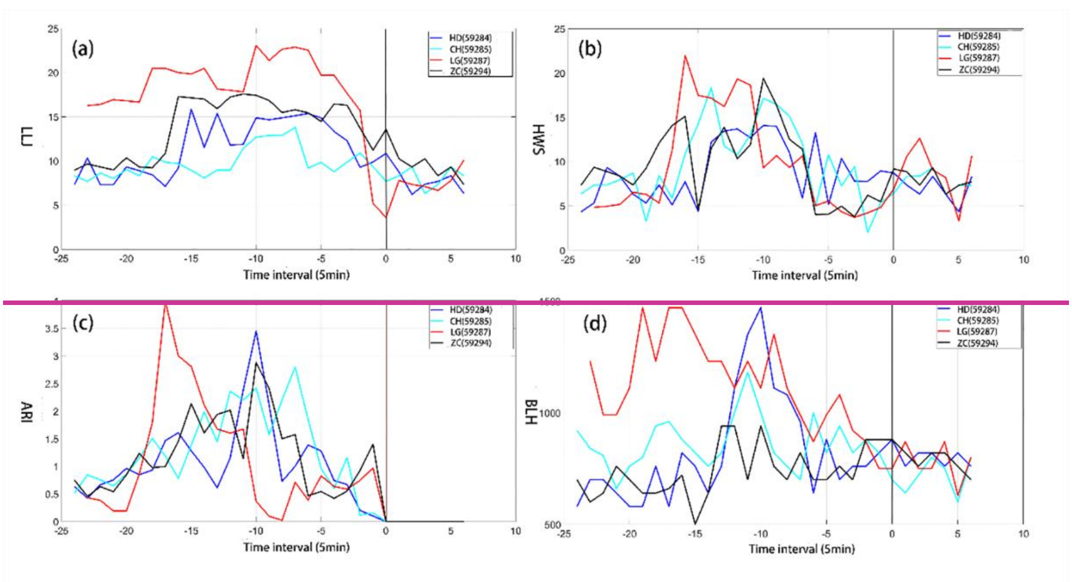

~~**Figure 15. Urban-rural variation of precursor signals for WSHR on April 20. The blue line represents Huadu station, the cyan line represents Conghua station, the red line represents Luogang station, and the black line represents Zengcheng station. (a) Low-level jet index (unit: 10^{-3} s^{-1}); (b) Horizontal wind shear (unit: 10^{-3} s^{-1}); (c) Atmospheric lifting intensity (unit: m km s^{-1}); (d) Boundary layer height (unit: m).**~~

~~Analyzing the wind profile characteristics of the four stations (Fig. 16), there is a westerly jet stream with wind speed larger than 16 m s^{-1} above 3km, which is SLJ. There is southerly wind with wind speed larger than 10 m s^{-1} at 1–2 km, which is BLJ. About 1 hour before rainfall, wind speed decreases at high altitudes and increases at low altitudes. Momentum is transferred from the upper layer to the lower layer, promoting the development of the BLJ. To explore the impact of this wind speed change on VWS, Figure 17 shows 3-hour average diagram of the vertical shear of the horizontal wind before precipitation at four wind profiler radar stations. Strong VWS areas appeared at all four stations before precipitation. The VWS is the strongest below 1 km, indicating that the LLJ in the boundary layer at the lower level is continuously strengthening. The strongest VWS is found at urban station (Fig. 17c).~~

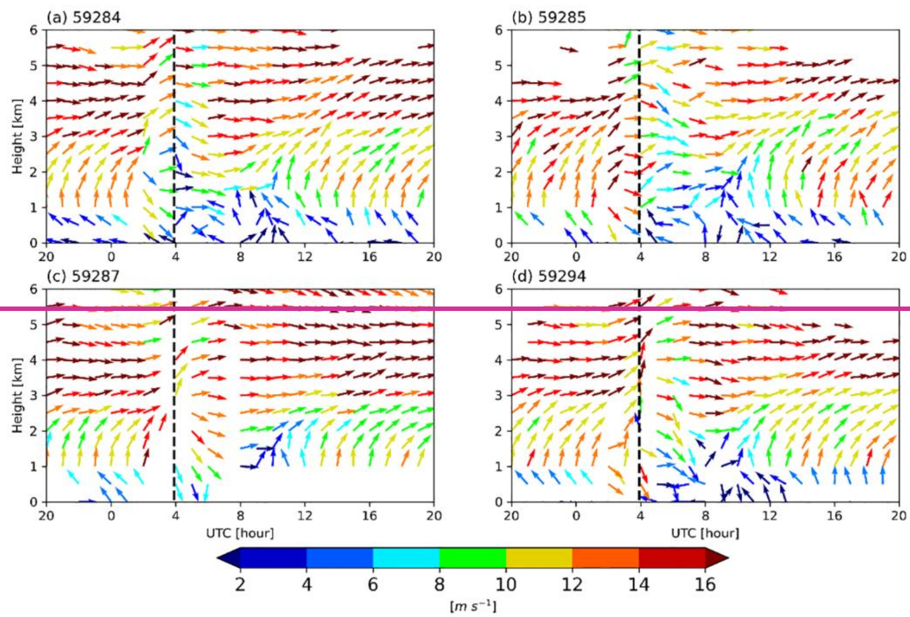

~~**Figure . Variation of horizontal wind field on April 20. (a) Huadu station; (b) Conghua station; (c) Luogang station; (d) Zengcheng station (vectors, unit: m s^{-1}, dashed line represents the rainfall onset time).**~~

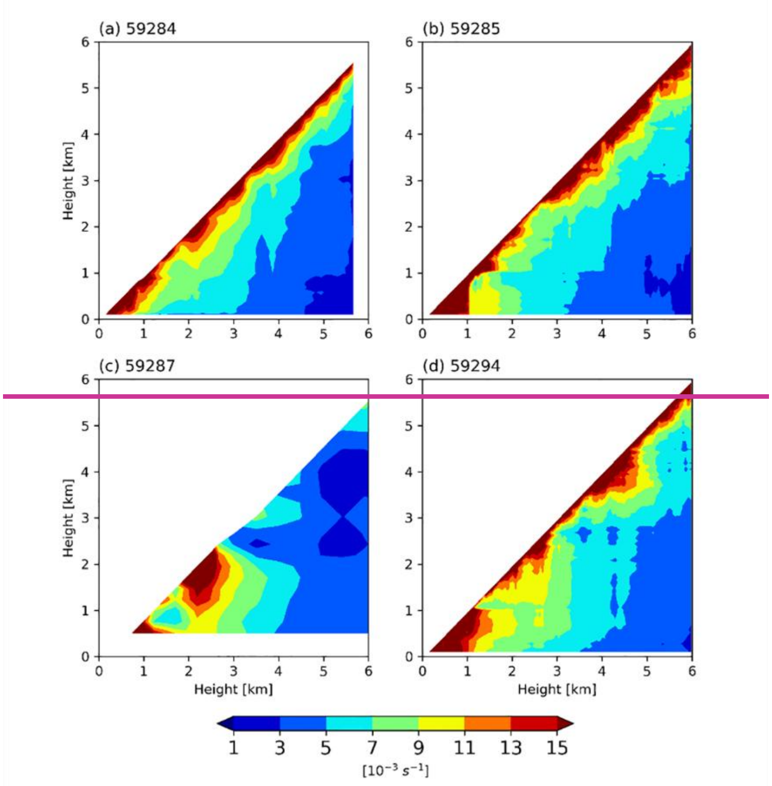

~~**Figure . As in Figure 6, here are (a) Huadu station; (b) Conghua station; (c) Luogang station; (d) Zengcheng station.**~~

~~To further explore the influence of jets on rainfall, the horizontal wind data from four wind profiler radars are used to calculate the vorticity and divergence at 1 km and 4 km, respectively (Fig. 18). Vorticity at 1 km in the suburban area is positive and the divergence is negative 2 hours before the precipitation occurs, indicating that the urban underlying surface in Guangzhou is conducive to the convergence of the offshore BLJ, and a large amount of warm, moist air from the sea converges in the lower layer of the city. The vorticity in the suburban area at 4 km is greater than that in the urban area, and the divergence in the urban area is greater than that in the suburban area, indicating that the wind speed of the SLLJ continues to increase after passing through the urban area. In comparison with suburban areas, urban centers are more conducive to the establishment of a structure characterized by low-level convergence and high-level divergence. Observations of stronger horizontal wind shear and atmospheric uplift can be made in urban areas before precipitation occurs.~~

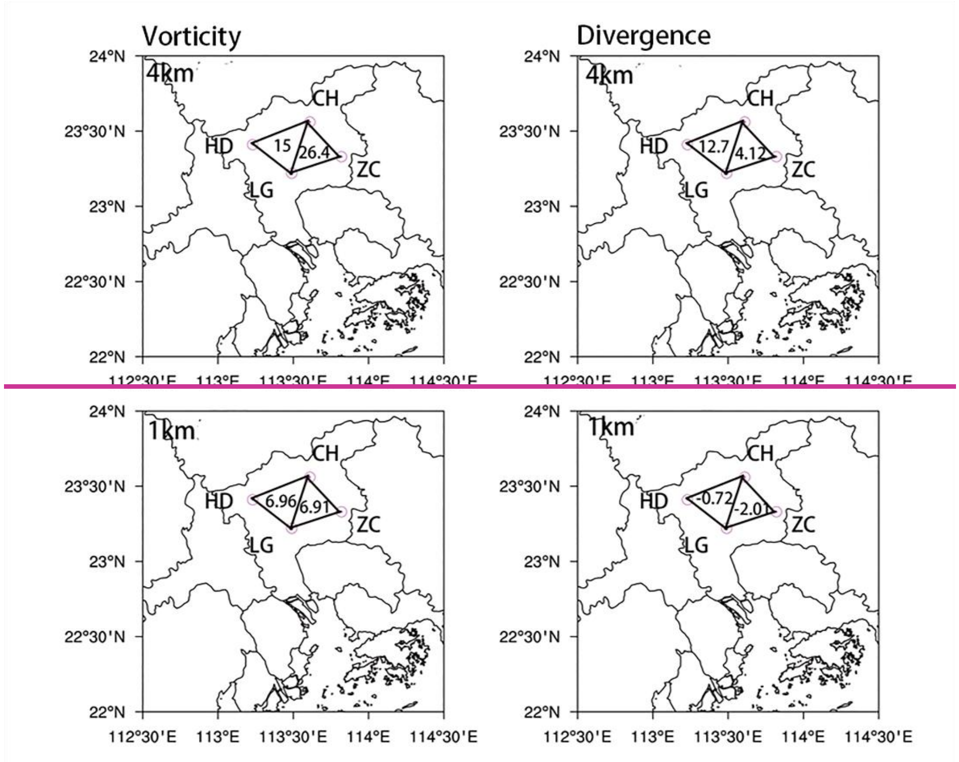

~~**Figure . Vorticity (unit: 10^{-5} s^{-1}) and divergence (unit: 10^{-5} s^{-1}) at heights of 1 km and 4 km in the Guangzhou suburban area, 2 hours before precipitation onset. (HD) Huadu station; (CH) Conghua station; (LG) Luogang station; (ZC) Zengcheng station.**~~

~~5 Discussion~~

~~5.1 Possible mechanisms of signal differences between regions~~

~~In recent years, many studies have investigated into the physical mechanisms of WSHR. Both Yangjiang and Shanwei are coastal areas, but their rainfall characteristics are different. Such difference is associated with dominant weather systems, water vapor and instability conditions, terrain forcing, and land-sea circulation (Chen et al., 2019). The spatial configuration of low-level water vapor transport has an important impact on the cumulative precipitation distribution of extreme mesoscale convective systems . The synergy of dual low-level jets, orographic lifting, and boundary-layer convergence lines performs a pivotal function in the occurrence of WSHR events (Liang and Gao, 2021; Pu et al., 2022; Zhang et al., 2022b). Moisture transport from the South China Sea to the Shanwei area is crucial for triggering warm-sector rainstorms . A study of an extreme case in the Guangzhou urban agglomeration found that the urban heat island effect, low-level convergence troughs, topography, and strengthening of low-level southerly winds are the key factors to trigger convection. The precipitation mechanism of WSHR varies spatially, and thus leads to significant inter-regional differences in the characteristics of the dynamical factors,~~

~~which can be attributed to the characteristics of the three main types of regions: western coast, central urban agglomeration, and eastern coast.~~

~~(1) In the western region, the WSHR is characterized by low-level warm, moist air convergence and orographic uplift. Wind profile analysis shows that southerly winds dominate below 2 km, within 2 hours prior to the heavy rainfall, while westerly winds prevail above 3 km. The clockwise rotation of wind direction reflects the warm advection process. Water vapor transport is mainly concentrated below 700 hPa, which triggers an upward movement under the effect of topography, resulting in a rapid enhancement of the ALI. Low-level water vapor convergence and upward moisture work together to form a pattern of low-level convergence and middle-level divergence. The increase in LLJI and VWS 30–60 minutes prior to the onset is conductive to heavy rainfall, showing that the development of low-level perturbations an obvious lower-level dominant mechanism.~~

~~(2) The WSHR in the central region typically occurs on the complex urban subsurface, with complex wind fields and earlier appearance of the precursor signals. Wind profiles show that there are double LLJs at 700 hPa and 900 hPa, where moisture transport and VWS are concentrated. a large low-level VWS due to the high roughness, rapidly weakening wind speeds below 1 km, and the presence of significant rapids between 2 and 4 km. The BLH is significantly enhanced in the urban center (LG), and starts to perturb and rise before the rainfall, and then falls. Evolutionary feature of initial ascent followed by descent reflects the accumulation and triggering process of energy within the boundary layer. Enhanced turbulent mixing strengthens local updrafts and leads to boundary layer lifting 3 hours prior to rainfall. Scattered convection may have already developed in the vicinity or upstream 1.5 hours before rainfall. Precipitation generated by this convection leads to evaporative cooling, forming cold pools, which were important in triggering and maintaining the MCSs . The outflow from these cold pools affects the local area, causing a rapid decrease in the BLH while lifting warm, moist air. The vertical transport term at 500–750 hPa shows upward motion, which is associated with coupling between the lower and upper jet streams. This manifests as a mechanism of low-level convergence and high-level divergence that facilitates rainfall formation.~~

~~(3) The eastern region is controlled by the South China Sea and the periphery of the subtropical high, exhibiting distinct characteristics of upper-level moisture transport. Wind profile analysis shows relatively weak low-level winds in this region, while a southwestward jet stream is active between 500–700 hPa. The moisture flux vector at this altitude shows an inclined upward pattern. Before precipitation, wind direction above 1 km is consistent with height, and vertical disturbances are relatively weak. Vertical moisture integration and flux analysis reveal that a wide range and strong intensity of moisture transport exists over this region. The upper-level jet stream dominates the rapid movement and accumulation of moisture, leading to a strong convergence zone in the lower levels and widespread divergence in the middle to upper levels, reflecting the mechanism of high-level control and low-level response. In addition, the LLJI is generally large and has a long duration in the eastern region, indicating that the persistent and stable jet stream contributes to steady moisture supply.~~

~~In conclusion, the genesis of WSHR in Guangdong manifests considerable regional disparity, predominantly attributable to variations in triggering mechanisms, altitudes of water vapor transport, and boundary layer properties. In the western sector, water vapor predominantly accumulates in the lower stratum, primarily elevated through orographic influences and convergence processes. The central region is characterized by a dual LLJ configuration. Rainfall is triggered by local thermal disturbances integrated with wind field coupling. The boundary layer height is most significantly affected by cities and changes of the BLH. Water vapor in the eastern region is mainly transported in the middle and upper layers, influenced by the upper-level jet and disturbances at the edge of the subtropical high.~~

~~5.2 Potential application of precursor signals in nowcasting~~

~~Quantitative precursor signals are extracted from wind profile radar data in high spatiotemporal resolutions, which provide a reference for advance nowcasting of the WSHR. It is found that most of the key meteorological factors begin to change significantly within 0.5–2 hours before the rainstorms, with obvious 'inflection point' characteristics: ALI uplift often occurs 60–90 minutes before precipitation; LLJI rapid intensification occurs 60–90 minutes before precipitation; BLH increase occurs about 80-100 minutes in advance; and increase in the BLH occurs about 80–100 minutes in advance. The rapid intensification of the LLJI occurs within 60–90 minutes; the BLH uplift process occurs about 80–100 minutes in advance, and the rapid change in VWS after a sustained increase indicates the release of vertical instability. These near-term changes are conductive for the short-term and nowcasting warning model of rainstorms.~~

~~6 Concluding Remarks~~

~~In this study, the precursor signals of the 2019 WSHR in Guangdong are systematically analyzed based on wind profile radar and high-density ground-based observational data. Results reveal the atmospheric dynamic processes before the occurrence of WSHR, and point out that there are significant seasonal and regional differences in the precursor signals of WSHR, which are mainly influenced by meteorological factors such as low-level jets, boundary layer height, atmospheric lifting intensity and vertical wind shear, and the signal characteristics in different regions are closely related to monsoon activities, geographical factors, etc. The main conclusions are shown as follows.~~

~~(1) Through analyzing the precursor signals of the wind field, vertical structure and boundary layer height in different regions, it can be seen that the warning signals of heavy rainfall in the warm sector usually appear 1–2 hours before the onset of rainfall and show different structural characteristics. Precipitation in the western region is influenced by low-level warm humid airflow and topographic uplift, and the signals are prominent in the lower layers. Rainfall in central region is influenced by urban effects and double low-level jets, and the signals are complex and occur earlier. Precipitation in the eastern region is influenced by high-altitude jets and water vapor transport, and the signals tend to be dominated by the upper layers.~~

~~(2) The main factors affecting regional differences in precursor signals are monsoon and geography. There is variability in the response to precursor signals in different regions. Precipitation in the western region relies more on low-level water vapor accumulation and topography; rainfall in the central region relies more on the urban heat island effect and boundary layer changes; and the precursor signals in the eastern region are more related to changes in high-altitude rapids and the oblique transport properties of water vapor. In addition, the activity of the summer monsoon in the South China Sea affects formation conditions of the WSHR, especially in enhancing water vapor transport and the development of low-level jets, which plays an important role in regulating the temporal and spatial distribution of the precursor signals.~~

~~(3) It is shown that the thermal and dynamical effects of urban agglomerations significantly change the boundary layer structure, which in turn affects the performance of the precursor signals. The urban heat island effect can advance the onset of boundary layer instability and enhance local instability and convective activity, making the precursor signals in the central region more localized and placing higher demands on nowcasting.~~

~~(4) Precursor signals have application potential in nowcasting. A refined forecast of heavy precipitation in different regions can be achieved by optimizing weights of regional precursor signals. In particular, the ability to forecast extreme precipitation can be significantly improved through developing a multi-factor composite forecasting system integrated with an intelligent early warning platform.~~

~~There are still some shortcomings in this study, the extraction thresholds and discrimination methods of precursor signals need to be standardized, the precursor signal characteristics of different types of WSHR have not been fully covered, and the study of urban dynamical mechanisms is still insufficient. In the future, the study will strengthen the exploration of the coupling mechanism of different scale dynamical processes, and further combine with machine learning and other methods, so that it can be more effectively used in storm forecasting operations.~~

Data availability

The ~~land cover~~LCZ data for Guangdong Province are available ~~at (Yang & Huang, 2021).~~from https://zenodo.org/records/7324909. The ERA5 data can be downloaded from https://cds.climate.copernicus.eu/datasets/reanalysis-era5-pressure-levels?tab=overview (Hersbach et al., 2023) and https://cds.climate.copernicus.eu/datasets/reanalysis-era5-single-levels?tab=download (Hersbach et al., 2023).

Author contributions~~.s~~

~~The study was completed with close cooperation between all authors. YY conceived of the idea for this work. ZH designed the methodology.~~ WL performed the main data analysis~~. WL~~ and ~~ZH drafted~~prepared the ~~original~~ manuscript ~~with contributions from SL, XB, YY.~~. ZH developed the precursor index calculations. SX contributed to data processing. LS, ~~SX, CL, YY~~XB and LY provided ~~useful~~ important scientific comments and suggestions ~~and comments for~~throughout the study. SL, YY (Yang Yang), CL and ~~helped revise~~JW contributed to the manuscript revision. SL provided expertise on wind profiler radar data quality assessment. YY (Yuanjian Yang) conceived of the study, provided overall scientific guidance, and supervised the project. All authors reviewed and approved the final manuscript.

Financial support

This work has been supported by the National Natural Science Foundation of China (grant nos. ~~42222503~~42521006, and 42175098), and Guangdong Provincial Marine Meteorology Science Data Center (grant no. 2024B1212070014).

Competing interests

The authors declare that there is no conflict of interest.

References

Bellamy, J. C.: Objective calculations of divergence, vertical velocity and vorticity, Bull. Amer. Meteor. Soc., 30, 45–49, https://doi.org/10.1175/1520-0477-30.2.45, 1949.

Chen, T. and Zhang, D.-L.: A 7-Year Climatology of Warm-Sector Heavy Rainfall over South China during the Pre-Summer Months, Atmosphere, 12, 914, https://doi.org/10.3390/atmos12070914, 2021.

Chen, Y., Chen, T., Wang, L., et al.: A review of the warm-sector rainstorms in China, Torrential Rain and Disasters, 38(5), 483－493, 2019.(in Chinese)

Demuzere, M., Kittner, J., Martilli, A., Mills, G., Moede, C., Stewart, I. D., van Vliet, J., and Bechtel, B.: A global map of

Local Climate Zones to support earth system modelling and urban-scale environmental science, Earth Syst. Sci. Data, 14, 3835–3873, https://doi.org/10.5194/essd-14-3835-2022, 2022.

Ding, Y. H.: Monsoons Over China. Dordrecht, Kluwer Academic, 419 pp, 1994.

Du, Y. and Chen, G.: Heavy rainfall associated with double low-level jets over southern China. Part I: Ensemble-based analysis, Mon. Wea. Rev., 146, 3827 – 3844, https://doi.org/10.1175/MWR-D-18-0101.1, 2018.

Du, Y., Zhang, Q., Ying, Y., and Yang, Y.: Characteristics of Low-level Jets in Shanghai during the 2008-2009 Warm Seasons as Inferred from Wind Profiler Radar Data, Journal of the Meteorological Society of Japan, 90, 891 – 903, https://doi.org/10.2151/jmsj.2012-603, 2012.

Du, Y., Chen, G., Han, B., Mai, C., Bai, L., and Li, M.: Convection Initiation and Growth at the Coast of South China. Part I: Effect of the Marine Boundary Layer Jet, Monthly Weather Review, 148, 3847 – 3869, https://doi.org/10.1175/MWR-D-20-0089.1, 2020a.

Du, Y., Chen, G., Han, B., Bai, L., and Li, M.: Convection initiation and growth at the coast of South China. Part II: Effects of the terrain, coastline, and cold pools, Mon. Wea. Rev., 148, 3871 – 3892, https://doi.org/10.1175/MWR-D-20-0090.1, 2020b.

Gao, Z., Zhu, J., Guo, Y., Luo, N., Fu, Y., and Wang, T.: Impact of Land Surface Processes on a Record-Breaking Rainfall Event on May 06 – 07, 2017, in Guangzhou, China, Journal of Geophysical Research: Atmospheres, 126, e2020JD032997, https://doi.org/10.1029/2020JD032997, 2021.

Heo, B., Jacoby-Koaly, S., Kim, K., Campistron, B., Benech, B., and Jung, E.: Use of the Doppler Spectral Width to Improve the Estimation of the Convective Boundary Layer Height from UHF Wind Profiler Observations, J. Atmos. Oceanic Technol., 20, 408–424, https://doi.org/10.1175/1520-0426(2003)020<0408:UOTDSW>2.0.CO;2, 2003.

Hersbach, H., Bell, B., Berrisford, P., Biavati, G., Horányi, A., Muñoz Sabater, J., Nicolas, J., Peubey, C., Radu, R., Rozum, I., Schepers, D., Simmons, A., Soci, C., Dee, D., and Thépaut, J.-N.: ERA5 hourly data on pressure levels from 1940 to present, Copernicus Climate Change Service (C3S) Climate Data Store (CDS) [data set], https://doi.org/10.24381/cds.bd0915c6, 2023.

Higgins, R. W., Yao, Y., Yarosh, E. S., Janowiak, J. E., and Mo, K. C.: Influence of the Great Plains low-level jet on summertime precipitation and moisture transport over the central United States, J. Climate, 10, 481 – 507, https://doi.org/10.1175/1520-0442(1997)010<0481:IOTGPL>2.0.CO;2, 1997.

Huang, S. S.: Heavy Rainfall over Southern China in the Pre-Summer Rainy Season, Guangdong Science and Technology Press, 244 pp., 1986. (in Chinese)

Huang, Y., Liu, Y., Liu, Y., Li, H., and Knievel, J. C.: Mechanisms for a Record – Breaking Rainfall in the Coastal Metropolitan City of Guangzhou, China: Observation Analysis and Nested Very Large Eddy Simulation With the WRF Model, JGR Atmospheres, 124, 1370 – 1391, https://doi.org/10.1029/2018JD029668, 2019.

Kotthaus, S., Bravo-Aranda, J. A., Collaud Coen, M., Guerrero-Rascado, J. L., Costa, M. J., Cimini, D., O’ Connor, E. J., Hervo, M., Alados-Arboledas, L., Jiménez-Portaz, M., Mona, L., Ruffieux, D., Illingworth, A., and Haeffelin, M.: Atmospheric boundary layer height from ground-based remote sensing: a review of capabilities and limitations, Atmos.

Meas. Tech., 16, 433 – 479, https://doi.org/10.5194/amt-16-433-2023, 2023.

Li, C., Zhang, X., Guo, J., Yu, Q., and Zhang, Y.: Decadal variation and trend of boundary layer height and possible contributing factors in China, Agricultural and Forest Meteorology, 347, 109910, https://doi.org/10.1016/j.agrformet.2024.109910, 2024a.

Li, N., Guo, J., Wu, M., Zhang, F., Guo, X., Sun, Y., Zhang, Z., Liang, H., and Chen, T.: Low-Level Jet and Its Effect on the Onset of Summertime Nocturnal Rainfall in Beijing, Geophysical Research Letters, 51, e2024GL110840, https://doi.org/10.1029/2024GL110840, 2024b.

Liang, Z. and Gao, S.: Organized Warm-Sector Rainfall in the Coastal Region of South China in an Anticyclone Synoptic Situation: Observational Analysis, J Meteorol Res, 35, 460 – 477, https://doi.org/10.1007/s13351-021-0157-4, 2021.

Liu, B., Guo, J., Gong, W., Shi, L., Zhang, Y., and Ma, Y.: Characteristics and performance of wind profiles as observed by the radar wind profiler network of China, Atmospheric Measurement Techniques, 13, 4589 – 4600, https://doi.org/10.5194/amt-13-4589-2020, 2020.

Liu, R., Sun, J., and Chen, B.: Selection and Classification of Warm-Sector Heavy Rainfall Events over South China, Chinese Journal of Atmospheric Sciences, 43(1), 119 – 130, doi:10.3878/j.issn.1006-9895.1803.17245, 2019.(in Chinese)

Liu, S. Y., Zheng, Y. G., and Tao, Z. Y.: The analysis of the relationship between pulse of LLJ and heavy rain using wind profiler data, J. Trop. Meteor., 19(3), 285 – 290, doi:10.3969/j.issn.1004-4965.2003.03.008, 2003.(in Chinese)

Lolli, S., Delaval, A., Loth, C., Garnier, A., and Flamant, P. H.: 0.355-micrometer direct detection wind lidar under testing during a field campaign in consideration of ESA’s ADM-Aeolus mission, Atmospheric Measurement Techniques, 6, 3349 – 3358, https://doi.org/10.5194/amt-6-3349-2013, 2013.

Luo, Y., Zhang, R., Wan, Q., Wang, B., Wong, W. K., Hu, Z., Jou, B. J.-D., Lin, Y., Johnson, R. H., Chang, C.-P., Zhu, Y., Zhang, X., Wang, H., Xia, R., Ma, J., Zhang, D.-L., Gao, M., Zhang, Y., Liu, X., Chen, Y., Huang, H., Bao, X., Ruan, Z., Cui, Z., Meng, Z., Sun, J., Wu, M., Wang, H., Peng, X., Qian, W., Zhao, K., and Xiao, Y.: The Southern China Monsoon Rainfall Experiment (SCMREX), https://doi.org/10.1175/BAMS-D-15-00235.1, 2017.

Ning, G., Luo, M., Bi, X., Liu, Z., Zhang, H., Huang, M., Huang, X., Yang, Y., and Wu, S.: Large-scale moisture transport and local-scale convection patterns associated with warm-sector heavy rainfall over South China, Atmospheric Research, 285, 106637, https://doi.org/10.1016/j.atmosres.2023.106637, 2023.

Pu, Y., Hu, S., Luo, Y., Liu, X., Hu, L., Ye, L., Li, H., Xia, F., and Gao, L.: Multiscale Perspectives on an Extreme Warm-Sector Rainfall Event over Coastal South China, Remote Sensing, 14, 3110, https://doi.org/10.3390/rs14133110, 2022.

Seibert, P., Beyrich, F., Gryning, S.-E., Joffre, S., Rasmussen, A., and Tercier, P.: Review and intercomparison of operational methods for the determination of the mixing height, Atmospheric Environment, 34, 1001 – 1027, https://doi.org/10.1016/S1352-2310(99)00349-0, 2000.

Stensrud, D. J.: Importance of low-level jets to climate: A review, J. Climate, 9, 1698 – 1711, https://doi.org/10.1175/1520-0442(1996)009<1698:IOLLJT>2.0.CO;2, 1996.

Stewart, I. D. and Oke, T. R.: Local Climate Zones for Urban Temperature Studies, Bull. Amer. Meteor. Soc., 93, 1879–1900, https://doi.org/10.1175/BAMS-D-11-00019.1, 2012.

Sun, J., Zhang, Y., Liu, R., Fu, S., and Tian, F.: A Review of Research on Warm-Sector Heavy Rainfall in China, Adv. Atmos. Sci., 36, 1299 – 1307, https://doi.org/10.1007/s00376-019-9021-1, 2019.

Trier, S. B., Davis, C. A., Ahijevych, D. A., Weisman, M. L., and Bryan, G. H.: Mechanisms supporting long-lived episodes of propagating nocturnal convection within a 7-day WRF model simulation, J. Atmos. Sci., 63, 2437 – 2461, https://doi.org/10.1175/JAS3768.1, 2006.

Wang, C., Chen, X., and Zhao, K.: Extreme local mesoscale convective systems over the South China coast during the warm season, Quart J Royal Meteoro Soc, e4959, https://doi.org/10.1002/qj.4959, 2025.

Wang, H., Luo, Y., and Jou, B. J.-D.: Initiation, maintenance, and properties of convection in an extreme rainfall event during SCMREX: Observational analysis, Journal of Geophysical Research: Atmospheres, 119, 13,206-13,232, https://doi.org/10.1002/2014JD022339, 2014.

Wu, N., Zhuang, X., Min, J., and Meng, Z.: Practical and intrinsic predictability of a warm-sector torrential rainfall event in the South China monsoon region, J. Geophys. Res.-Atmos., 125, e2019JD031313, https://doi.org/10.1029/2019JD031313, 2020.

Wu, Y., Guo, J., Chen, T., and Chen, A.: Forecasting Precipitation from Radar Wind Profiler Mesonet and Reanalysis Using the Random Forest Algorithm, Remote Sensing, 15, 1635, https://doi.org/10.3390/rs15061635, 2023.

Xian, T., Guo, J., Zhao, R., Guo, X., Li, N., Sun, Y., Zhang, Z., Su, T., and Li, Z.: Impact of Urbanization on Mesoscale Convective Systems: Insights From a Radar Wind Profiler Mesonet, Theoretical Analyses, and Model Simulations, Journal of Geophysical Research: Atmospheres, 129, e2024JD042294, https://doi.org/10.1029/2024JD042294, 2024.

Zeng, W., Chen, G., Du, Y., and Wen, Z.: Diurnal variations of low-level winds and precipitation response to large-scale circulations during a heavy rainfall event, Mon. Wea. Rev., 147, 3981 – 4004, https://doi.org/10.1175/MWR-D-19-0131.1, 2019.

Zhang, L., Ma, X., Zhu, S., Guo, Z., Zhi, X., and Chen, C.: Analyses and applications of the precursor signals of a kind of warm sector heavy rainfall over the coast of Guangdong, China, Atmospheric Research, 280, 106425, https://doi.org/10.1016/j.atmosres.2022.106425, 2022a.

Zhang, M. and Meng, Z.: Warm-sector heavy rainfall in southern China and its WRF simulation evaluation: A low-level-jet perspective, Mon. Wea. Rev., 147, 4461 – 4480, https://doi.org/10.1175/MWR-D-19-0110.1, 2019.

Zhang, M., Rasmussen, K. L., Meng, Z., and Huang, Y.: Impacts of Coastal Terrain on Warm-Sector Heavy-Rain-Producing MCSs in Southern China, Monthly Weather Review, 150, 603 – 624, https://doi.org/10.1175/MWR-D-21-0190.1, 2022b.

Zhong, S. and Chen, Z.: The Impacts of Atmospheric Moisture Transportation on Warm Sector Torrential Rains over South China, Atmosphere, 8, 116, https://doi.org/10.3390/atmos8070116, 2017.

Zhou, X., Cheng, Z., Li, H., and Hu, D.: Comparison between the Roles of Low-Level Jets in Two Heavy Rainfall Events over South China, J Meteorol Res, 36, 326 – 341, https://doi.org/10.1007/s13351-022-1159-6, 2022.